1	Title:
2	Inferring Long-Term Tectonic Uplift Patterns from Bayesian Inversion of Fluvially-Incised
3	Landscapes
4 5 6	Bar Oryan ^{1*} , Boris Gailleton ² , Jean-Arthur Olive ³ , Luca C. Malatesta ⁴ and Romain Jolivet ^{3,5}
7	Affiliations:
8	(1)Scripps Institution of Oceanography, UC San Diego, La Jolla, CA 92093,USA
9	(2)Univ. Rennes, Géosciences Rennes, UMR 6118, 35000 Rennes, France.
LO	(3)Laboratoire de Géologie, École normale supérieure – PSL, CNRS UMR 8538, Paris, France.
l1	(4)Earth Surface Process Modelling, GFZ German Research Center for Geosciences, Potsdam
L2	Germany.
L3	(5)Institut Universitaire de France, 1 rue Descartes, 75006 Paris.
L4	
L5 L6	Corresponding author: Bar Oryan (bar.oryan@columbia.edu)

17 **Abstract**

18

19

20

21

22

23

24

25

26

27

28

29

30

31

32

33

Earth surface processes encode the combined forcing of tectonics and climate in topography. Separating their contributions is essential for using landscapes as quantitative records of crustal deformation. Here, we develop a method to invert non-dimensionalized, spatially variable fields of long-term rock uplift and rock erodibility from fluvially incised landscapes, using an extended χ -coordinate system that accounts for variability in uplift, erodibility, and precipitation (χ_{UKO}). We invert 170 synthetically-generated landscapes and demonstrate that our method accurately recovers the spatial variability of rock uplift and rock erodibility, even when applied to settings that deviate from the ideal model of equilibrated, detachment-limited channels, which underpins the χ_{UKO} framework. We subsequently apply our inversion to six natural landscapes shaped by normal faults (half-grabens), and to a 200-km wide region of the central Himalayas. We show that our inversion can resolve the effect of climate and lithology while extracting uplift fields that are consistent with patterns expected from upper crustal flexure and previous estimates derived from geomorphological markers. The success of our method in recovering rock uplift patterns, isolated from the effects of climate and erodibility, highlights its applicability to settings where long-term uplift trends are unknown, paving the path to deciphering tectonic fingerprints recorded in landscapes over tens of thousands of years.

Plain Language Summary

Earth's topography is uniquely shaped by both deep tectonic activity and the erosive processes that sculpt its surface. Utilizing these landscapes to deduce tectonic activity presents valuable insights, albeit elusive. In this study, we introduce a mathematical inversion method utilizing geomorphic indices to extract tectonic uplift patterns from landscapes. We assess the method's effectiveness on synthetic landscapes that incorporate surface processes our model does not explicitly account for. Our findings confirm that the method can accurately retrieve rock uplift rate patterns, even in landscapes not solely governed by steady state detachment-limited erosion—the assumption underlying our inversion technique. Applying this method to natural landscapes shaped by normal faults and the Himalayas, we demonstrate that our extracted uplift patterns align with expected patterns of tectonic warping. This approach sets the stage for using river incised topography to decipher tectonic signals accumulated over tens of thousands of years.

Key Points

- New method infers unknown spatial rock uplift patterns and variable erodibility from fluvial landscapes using a Bayesian approach.
 - Synthetic tests reveal the broad applicability of our method, even when deviating from the steady-state detachment-limited incision.
 - Inverting seven landscapes yields uplift fields consistent with previous estimates and patterns expected from upper crustal warping

1 Introduction

56

57

58

59

60

61

62

63

64

65

66

67

68

69

70

71

72

73

74

75

76

77

78

79

80

81

82

83

84

In Earth's most tectonically active regions, topography reflects a dynamic balance between crustal deformation and climate-modulated surface processes. The first induces vertical motion of the surface through processes such as faulting, dynamic topography and isostasy (e.g., Faccenna et al., 2019; King et al., 1988; Watts, 2001) while the latter incise and rework relief by eroding bedrock and transporting and depositing the resulting sediments (e.g., Merritt et al., 2003). Thus, the shape of landscapes represents a snapshot of the ever-evolving competition of these two processes (Kirby & Whipple, 2012; Molnar & England, 1990; Willgoose et al., 1991).

Disentangling the contributions of climate and tectonics on surface topography is a crucial goal of tectonic geomorphology (e.g., Armijo et al., 1996; Gallen et al., 2023; Lavé & Avouac, 2001; Malatesta et al., 2021). Extracting spatial patterns of rock uplift rates from landscapes is particularly important as it provides indirect quantitative constraints on the underlying tectonic mechanisms and their persistence over geological timescales. For instance, in landscapes shaped by normal faults, spatially-varying vertical rock uplift is used to estimate the effective elastic thickness of the lithosphere (Armijo et al., 1996). The morphology of fault scarps may provide insights into the seismogenic properties of underlying faults (e.g., Holtmann et al., 2023). Another compelling example for the importance of landscapes in recording tectonic processes is the fact that short-term fault locking can leave a lasting imprint on forearc topography over tens of earthquake cycles (Cattin & Avouac, 2000; Cooke et al., 2025; Dublanchet & Olive, 2024; Jolivet et al., 2020; Malatesta et al., 2021; Meade, 2010; Oryan et al., 2024). Nonetheless, extracting rock uplift fields from landscapes is challenging especially in the absence of thermochronological data or geomorphological markers. Current approaches (e.g., Castillo et al., 2014; Densmore et al., 2007; Ponza et al., 2010; Su et al., 2017) often rely on the stream power incision model (Howard & Kirby, 1983) utilizing a landscape metric called the steepness index, k_{sn} (Wobus et al., 2006, See section 2 for definition). While useful, k_{sn} is interpreted as sensitive to the ratio of rock erodibility to rock uplift which may be strongly skewed by spatial variations in rock erodibility, a quantity that is difficult to constrain. Furthermore, it depends on point measurements of surface slopes, which can be noisy (Gailleton et al., 2021). On the other hand, the χ metric, which integrates upstream changes in drainage area normalized by the concavity index across entire

river networks, provides a quantitative alternative to recover spatial variations in rock uplift rates from landscapes (Perron & Royden, 2013). Previous work has employed the χ metric for landscape inversion focusing on uplift rate history, while largely neglecting spatial variations in rock uplift (Croissant & Braun, 2014; Fox et al., 2014; Goren et al., 2014; Goren et al., 2022; Pritchard et al., 2009; Smith et al., 2024).

Here we invert landscapes to recover spatially variable patterns of rock uplift, while simultaneously solving for spatial variations in erodibility (linked to lithology) and accounting for climatic effects (Fig. 1). To our knowledge, this is the first attempt to infer spatially variable rock uplift fields directly from landforms. We accomplish this by extending the χ metric and applying a Bayesian quasi-Newton inversion scheme, which constructs fields of rock uplift and erodibility using B-spline interpolation functions in a manner that minimizes the misfit between measured and modeled river elevation profiles in χ -space. We test the strengths and limitations of our method using synthetic landscapes and demonstrate its ability to recover rock uplift patterns and erodibility values while accounting for climatic effects. Subsequently, we apply our method to seven natural landscapes shaped by divergent and convergent tectonics to demonstrate its effectiveness in real-world scenarios.

2 Inferring tectonic uplift from landscapes within the stream power framework

2.1 The detachment-limited stream power model

The stream power incision model posits that the erosion rate of a riverbed at a certain point is linked to water flux (captured by proxy through drainage area A), channel slope $(\frac{dz}{dx})$ and the erodibility of the material (K) (Hack, 1973; Howard & Kerby, 1983). To maintain a uniform rate of erosion, the river gradient diminishes downstream as drainage area increases, resulting in a concave river profile. According to this model, the change in elevation over time t, of a river eroding at rate, E, under rock uplift, U, is described as follows:

1.
$$\frac{\partial z(x,y,t)}{\partial t} = U(x,y,t) - E(x,y,t) = U(x,y,t) - K(x,y,t)A^{m}(x,y,t) \left(\frac{\partial z}{\partial x}\right)^{n}$$

113114

- Where m and n are constants and (x,y) is position, hereafter denoted as \vec{x} for concision (See Table
- 116 1 for definitions of all parameters throughout the manuscript).
- The rate, $c(\vec{x})$, at which a local perturbation in topography travels upstream (i.e., the celerity of
- 118 knickpoint migration) is linked to the local erodibility, drainage area and topographic gradient
- 119 (Rosenbloom & Anderson, 1994; Whipple & Tucker, 1999):

120

121
$$2. c(\vec{x}) = K(\vec{x})A(\vec{x}) \left(\frac{dz(\vec{x})}{dx}\right)^{n-1}$$

- The time for this perturbation, manifested as a knickpoint, or a sharp step in the river profile, to
- travel from the river base upstream to point x_s is given by (Whipple & Tucker, 1999):

124

125 3.
$$\tau(x_s) = \int_0^{x_s} \frac{dx}{c(\vec{x})} = \int_0^{x_s} \frac{dx}{K(\vec{x})A(\vec{x})\left(\frac{dz(\vec{x})}{dx}\right)^{n-1}}$$

126

- 127 At steady state, when erosion balances rock uplift, the equilibrium channel slope follows an
- inverse power-law relationship with drainage area:

129

$$4. \quad \frac{dz}{dx} = k_{sn}A(\vec{x})^{-\theta},$$

- where $k_{sn} = \left(\frac{U(\vec{x})}{\kappa(\vec{x})}\right)^{\frac{1}{n}}$ is the nondimensional channel steepness index, typically used as a proxy
- 132 for rock uplift rate, and $\theta = \frac{m}{n}$ is known as the concavity index.

133

- 2.2 The integral approach: river profiles in γ -space
- Upstream integration of equation 4 from an arbitrary base level x_b results in (Perron &
- 136 Royden, 2013):

$$5. \quad z(\vec{x}) = z(x_b) + a_s \cdot \chi(\vec{x})$$

138 Where,

139 6.
$$\chi = \int_{x_b}^{x} \frac{dx}{A^*(\vec{x})^{\frac{m}{n}}}; a_s = \left(\frac{U_0}{K_0 A_o^m}\right)^{\frac{1}{n}},$$

 A_o is a constant reference drainage area such that $A^*(x) = \frac{A(x)}{A_0}$ is dimensionless and U_0 141 and K_0 denote constant uplift and erodibility values. The integral along x here denotes an 142 upstream path to a connected network of tributaries.

This coordinate transformation allows us to describe river profiles in terms of χ and z (Fig. 1). In the case of spatially uniform U and K, stream profiles in χ -space will exhibit a linear relationship between the two variables, characterized by a slope a_S . In landscapes where erodibility and rock uplift vary spatially , the definition of χ can be amended as (Olive et al., 2022; Perron & Royden, 2013):

148
$$7. \quad \chi_{UK} = \int_{x_b}^{x} \left(\frac{U^*(\vec{x})}{A^*(\vec{x})^m K^*(\vec{x})} \right)^{\frac{1}{n}} dx \; ; \; a_S = \left(\frac{U_o}{K_o A_o^m} \right)^{\frac{1}{n}}$$

In this case, U_0 and K_0 are reference values so the trailing terms are dimensionless ($U^* = \frac{U}{U_0}$, $K^* = \frac{K}{K_0}$) and χ_{UK} denotes a version of χ corrected for known spatial variations in uplift rate and erodibility.

In the general case where water flux is not proportional to drainage area alone but varies due to a spatially heterogeneous precipitation rate, $P(x) = P_0 P^*(x)$, the adjusted discharge rate, $A_Q(x)$, is given by (Babault et al., 2018; Leonard et al., 2023; Leonard & Whipple, 2021):

155 8.
$$A_Q(x) = \int_{x_b}^{x} P(x) dA = A_Q^*(x) A_{0Q}$$

Where $A_{0Q} = P_0 A_0$ is a reference value so $A_Q^*(x)$ is dimensionless.

In this case, the χ_{UK} coordinate (eq. 7) can be reformulated by substituting the reference values A_{0Q} for A_0 and precipitation-weighted contributing area A_Q^* for the drainage area A^* , resulting in the precipitation-adjusted form χ_{UKQ} . When the dimensionless fields $U^*(\vec{x})$, $K^*(\vec{x})$ and $P^*(\vec{x})$ are all properly accounted for, the steady state landscape will verify equation (5) and river

161 elevation will correlate linearly with χ_{UKQ} (Fig. 1), a relationship that can be exploited using an inverse framework.

3 Inverting rock uplift pattern from river incised landscapes

164 3.1 Forward model

3.1.1 Parameter space, data space and cost function

The detachment-limited stream power model in χ_{UKQ} -space provides a robust framework to invert a spatial pattern of rock uplift $U^*(\vec{x})$ from river-incised landscapes. We first outline the direct (forward) problem of river profiles in χ_{UKQ} -space, given the parameters $m, n, a_s, U^*(\vec{x})$ and $K^*(\vec{x})$. This is done by computing χ_{UKQ} , and modeled river elevation, z_m , using eq. 5, as:

9.
$$z_m = z_b + a_s \cdot \chi_{uKQ}(m, n, U^*, K^*) = g(a_s, m, n, U^*, K^*)$$

We estimate the robustness of our direct model, expressed through the function g, by computing the difference between modeled elevation, z_m , and measured elevation, z_{obs} , typically obtained from a digital elevation model (DEM), using the cost function, ϕ , built with the L2 norm:

178
$$10. \ \phi(m, n, a_s, U^*, K^*) = ||g(a_s, m, n, U^*, K^*) - z_{obs}||_2$$

3.1.2 Parameterizing rock uplift patterns using B-spline functions

We parameterize the spatial variability of rock uplift, $U^*(\vec{x})$, using B-spline functions (Agrapart & Batailly, 2020; De Boor, 1978; Piegl & Tiller, 1997). Constructed from a series of piecewise polynomial basis functions and defined between a grid of control points referred to as knots, B-splines serve as interpolating functions where a coefficient at each knot controls the shape of the rock uplift pattern (See Text S1). This approach provides the flexibility to modify uplift patterns by simply adjusting the coefficient values without being restricted to a

predetermined functional form, thus ensuring a smooth and continuous representation of spatial variability in rock uplift.

Importantly, our B-spline uplift parameterization can be applied in two modes. In the one-dimensional (1D) configuration, knots are arranged along a single transect, allowing rock uplift to vary in one direction while remaining constant in the orthogonal direction. In the two-dimensional (2D) configuration, knots are distributed across a spatial grid, enabling uplift to vary freely in both horizontal dimensions. This allows us to represent both, directionally constrained 1D uplift patterns and fully heterogeneous 2D fields using the same smooth, continuous interpolation scheme.

3.1.3 Parameterizing spatial Erodibility

Spatial variations in erodibility are typically driven by contrasts in lithology (Campforts et al., 2020; Ellis & Barnes, 2015; Gailleton et al., 2021; Harel et al., 2016), often marked by the occurrence of major faults. Thus, using continuous mathematical functions, such as B-splines, polynomials, or Gaussians, to represent variations in erodibility would misrepresent the inherently piece-wise nature of this field. We instead delineate lithological units (e.g., from geological maps) and invert for their piece-wise uniform erodibility k_i across various lithological domains (numbered by i). As for the rock uplift pattern, it should be noted that we invert for relative erodibility K^* rather than for absolute erodibility.

3.2 Inversion scheme

To identify plausible combinations of a_s , m, n, U^* and K^* , we minimize the misfit between the modeled and measured elevation (eq. 9) using a Bayesian quasi-Newton scheme (Tarantola, 2005) in an iterative fashion:

Where p_l is a vector comprising all model parameters at iteration l. G^l is the Jacobian matrix at step I determined using centered finite difference such that:

219
$$12. G_{ij}^l = \frac{\partial g_i}{\partial p_j}$$

 z_{obs} is a vector of observations consisting of measured elevation z, z_m is the modeled elevation of rivers computed using $g(p_l)$, C_M is the a priori covariance matrix, C_D is the observation covariance matrix, and μ is a constant between 0 and 1.

We employ an initial guess, p_o , assuming m=0.5, n=1, a_s = 0.1 as well as B-spline and erodibility coefficients that describe uniform rock uplift and erodibility patterns. These initial values reflect commonly used stream power parameters observed in natural landscapes (Gailleton et al., 2021; Mudd et al., 2014; Snyder et al., 2000), with uniform uplift and erodibility providing a neutral baseline for the inversion. We set the prior covariance matrix C_m with diagonal terms equal to 0.01 (standard deviation of 0.1) for the entries corresponding to m, n, and a_s , and 1 for B-spline weights and dimensionless erodibility coefficients, reflecting greater uncertainty in spatial heterogeneity. At each iteration, the inversion dynamically updates all parameters including m, n, a_s via the Bayesian quasi-Newton step (eq. 11), which incorporates the prior covariance, the model sensitivity matrix, G_n , and the data misfit ($z_m - z_{obs}$) weighted by the observation covariance, C_D . Lastly, we consider reaching convergence at step l when $\frac{\phi(p_l)-\phi(p_{l-1})}{\phi(p_o)} < 0.01$.

Upon reaching convergence and a satisfying solution, we can use the recovered B-spline parameters to describe the rock uplift pattern along rivers used in the inversion as well as across the entire rectangular domain bounded by the river network (Text S1). However, the geometry of the river network may leave some B-spline knots poorly constrained due to the absence of nearby rivers. To address this, we compute rock uplift only within catchments feeding the rivers used in our analysis and ensure that the employed knots have non-negligible values based on the sensitivity parameter computed using the diagonal of the product of G^TT .

Finally, we emphasize that our inversion recovers the dimensionless rock uplift pattern, (U^*) and the dimensionless erodibility field (K^*) , rather than their absolute magnitudes in physical

units. This is because the inversion determines only the $\chi_{UKQ}-slope$ (= a_s) and cannot independently resolve the reference uplift rate U_0 or erodibility K_0 (see Section 2.2 for more details). Constraining either parameter would require in situ measurements and lies beyond the scope of this study.

4 Application to synthetic landscapes

We assess the reliability of our methodology—which inherently assumes steady-state channel incision—across a range of synthetic landscapes. These artificial terrains are generated using the stream power law and include varying degrees of deviation from pure detachment-limited steady conditions by incorporating sediment transportation, hillslope diffusion, orographic precipitation, spatial variations in erodibility, and temporal changes in rock uplift rates, as described in detail in the following section(e.g., Leonard & Whipple, 2021; Merritt et al., 2003; Roering et al., 1999, 2001; Whipple, 2009).

4.1 Generating synthetic landscapes

We model synthetic terrains, incorporating both fluvial and hillslope erosion along with deposition dynamics based on the CIDRE model framework defined by (Carretier et al., 2016). In this framework, elevation z varies in time such as

265
$$13. \frac{dz}{dt} = \dot{d}_f - \dot{e}_f + \dot{d}_h - \dot{e}_h + U(\vec{x})$$

where \dot{d}_f is the fluvial deposition rate, $\dot{e_f}$ the fluvial incision rate, \dot{d}_h the hillslope diffusion flux, $\dot{e_h}$ the hillslope erosion rates and $U(\vec{x})$ is the imposed tectonic uplift. The fluvial component relies on a formulation originally developed by Davy & Lague (2009) where erosion and sediment entrainment are functions of stream power and sediment transport deposition. The hillslope laws are a hybrid between linear and non-linear landscape diffusion models, reproducing both endmembers by separating the erosion and deposition processes. The erosion term is linear to the

slope, while the deposition term encompasses the non-linearity function of the critical slope (see Carretier et al., 2016 for full details). Both feed and deplete a sediment flux – that we report as the flux entering each cells in this manuscript.

We use an explicit finite difference numerical scheme to solve equation (13) where spatial discretization is done along a 100 X 100 km regular 2D grid with 400 m spacing in the x and y directions. We use different graph theory algorithms to organize our nodes into an upstream to downstream topological order (see Gailleton et al., 2024 for full method description) and use the carving algorithm of Cordonnier et al., (2019) to resolve local minima. We use a time step of 500 years and run the synthetic models for 5 million years to ensure the landscape reaches a topographic steady state, with less than 1 meter of mean elevation change between consecutive time steps. Lastly, we use n=1, m=0.45, consistent with typical values observed in natural landscapes (Gailleton et al., 2021), and set the base uplift rate, U_0 to $1.2 \ mm \cdot yr^{-1}$ which lies within the range observed in forearc landscapes (e.g., Burbank et al., 2003; Gallen et al., 2023; Godard et al., 2014; Herman et al., 2010; Melnick, 2016). The erodibility coefficient K is set to $2 \cdot 10^{-5} \ m^{0.9} yr^{-1}$ to produce approximately 1 km of maximum relief in our synthetic landscape, roughly the average relief in the normal fault landscapes we analyze. Lastly, we parameterize the imposed tectonic uplift field using an asymmetrical 2-D Gaussian function:

14.
$$U(x,y) = U_0 \cdot exp \left[-a(x - x_0) + 2b(x - x_0)(y - y_0) + c(y - y_0)^2 \right]$$

Where
$$a = \frac{\cos^{2(\beta)}}{2\sigma_x^2} + \frac{\sin^{2(\beta)}}{2\sigma_y^2}$$
, $b = -\frac{\sin(2\beta)}{4\sigma_x^2} + \frac{\sin(2\beta)}{4\sigma_y^2}$, $c = \frac{\sin^{2(\beta)}}{2\sigma_x^2} + \frac{\cos^{2(\beta)}}{2\sigma_y^2}$, β is the azimuth of the long-axis of the Gaussian, x_o , σ_x and y_o , σ_y are the center and width of the gaussian along

the x and y directions, respectively.

4.2 Inversion of synthetic landscapes

We apply our inversion scheme on synthetic landscapes corresponding to the final step of our numerical simulations and select the 8000 most downstream nodes from the largest catchments to guarantee our inversion outputs are not secondarily influenced by the number of observations (z_{obs}). To mimic the uncertainty in real elevation data we add noise using randomly

sampled values from a normal distribution centered around 0 with standard deviation, ε , of 10 m. We then apply our inversion method to the resulting landscapes and evaluate its performance by comparing the inverted uplift and elevation (eq. 8) to the imposed uplift and the measured synthetic elevation at the final time step, using the root mean square (RMS) misfit:

307
$$15. RMS = \sqrt{\frac{1}{N} \sum_{i=0}^{N} (q_i^r - q_i^m)^2}$$

Where q_i^r is inverted value i, q_i^m measured (or imposed) value i and N total number of measurements in the dataset.

4.3 Results

4.3.1 Detachment-limited scenario

We first test our inversions by generating two exclusively detachment-limited synthetic landscapes. The first landscape is subject to a pattern of rock uplift that decreases exponentially from west to east (x-axis), and is uniform along the y-axis (1-D case;Fig. 2A1) while the second landscape experiences a 2D-varying uplift pattern based on an ellipsoidal function (Fig. 2A2;Table S1; Fig. S1). We simulate the evolution of these landscapes until they reach steady state then apply 3 inversion approaches: (1) 1D inversion applied to the 1-D uplift landscape, (2) 2-D inversion applied to the 2D uplift landscape (see section 3.1.2), and (3) inversion for landscapes constants assuming uniform rock uplift for both cases.

Both our 1-D and 2-D inversions that account for varying rock uplift perform well, retrieving landscape constants (Figs. 2B1 & B2) and uplift patterns that are nearly identical to the imposed ones (Figs. 2A1, 2A2, 2C, and 2D). The RMS error between the inverted and imposed uplift is 0.01 for both the 1-D and 2-D cases, indicating that the inferred uplift closely matches the imposed uplift signal across the 8,000 river nodes used. Additionally, the inverted elevation closely mirrors the true elevation, with discrepancies primarily reflecting the introduced noise, ε , resulting in an RMS error of approximately 10 meters (Fig. 2B1 & 2B2). This accuracy is further illustrated by the near-linear shape of the final river elevation profiles in χ_{uKQ} -space, where scatter around the linear trend reflects the added noise (Fig. 2C). In contrast, the inversion

assuming uniform rock uplift returns RMS values that are 3-7 times higher and fails to accurately determine landscape constant m, n and a_s (Figs. 2B1 & B2).

This successful recovery is unsurprising, given that the landscapes were generated using the detachment-limited model which underlies our forward modeling. In this idealized setup, testing mainly verifies that the forward and inverse models are implemented consistently. Once we have established this, we proceed to test the limitations of our inversion approach by challenging the assumptions it relies on.

4.3.2 Scenarios deviating from the Detachment-limited endmember

4.3.2.1 Sediment transport length

We apply our inversion scheme to synthetic landscapes featuring varying degrees of sediment deposition, hillslope diffusion, orographic effects, spatial variations in erodibility, and temporal changes in uplift rates. For the sediment deposition case, we generate 20 identical landscapes that vary only in their characteristic sediment transport length, which controls the distance over which sediments are deposited. Low values, characteristic of harder-to-mobilize sediments, produce transport-limited behavior, whereas high values, typical of systems where sediment is evacuated efficiently, lead to detachment-limited conditions. In natural settings, this parameter primarily reflects sediment grain size, with coarser sediment corresponding to shorter transport lengths (e.g., Carretier et al., 2016;Davy and Lague,2009, Merritt et al., 2003).

For transport lengths larger than 1 km, our inversion accurately recovers landscape parameters with RMS elevation and uplift values comparable to the noise we added, ε (Figs. 3A1 & 3B1). Landscapes characterized by transport length smaller than 1 km generate greater relief owing to the additional sediment deposition. Consequently, inverting these models yields less accurate inversion results, with RMS values 5 to 30 times higher for both elevation and uplift (Figs. 3A1 & 3B1). Interestingly, even as the landscape deviates significantly from the detachment-limited case, the inversion aims to maintain the imposed $\frac{m}{n}$ ratio, capturing this "detachment-limited property" of the landscape (Fig. S2).

4.3.2.2 Diffusion

To test the effect of hillslope diffusion on our inversion, we model and invert 50 landscapes, each employing a distinct diffusion parameter controlling topographic dispersion across the landscapes (Carretier et al., 2016). For diffusivities smaller than $10^{-2}\ m^2\cdot yr^{-1}$ the inversion retrieves the imposed landscape parameters with negligible RMS misfit, indicating agreement between retrieved and imposed parameters (Fig. 3A2). For diffusivity values of $10^{-2}-10^{-1}m^2\cdot yr^{-1}$, the retrieved rock uplift exhibits pronounced uncertainties but still captures the original signal (Fig. 3B2). For diffusivities $> 10^{-2}\ m^2\cdot yr^{-1}$, the river network ceases to resemble a typical mountain drainage system (Fig. S3) and fails to produce continuous channels in the center of the domain. This is reflected in the poor performance of the inversion showing RMS values 10-30 times higher than base RMS level (Fig. 3A2).

4.3.2.3 Precipitation

Spatial variability in climatic conditions can also significantly influence landscapes (e.g., Molnar & England, 1990), particularly in mountain ranges with orographic precipitation on the windward flanks and drier conditions on the leeward sides (e.g., Bookhagen & Burbank, 2010). To incorporate this effect into the evaluation of our synthetic models , we index precipitation on elevation using the equation $P(z) = P_{\rm sl} e^{-\frac{z}{h_0}}$, where $P_{\rm sl}$ is precipitation at sea level, z elevation, and h_0 a reference elevation (Hergarten & Robl, 2022). To reflect reduced rainfall along the lee side of the landscape we reduce the h_o value there, effectively generating uneven precipitation P(x,z) (e.g., Figs. 3B3, S3D1 and S3D2). We then simulate 50 landscapes using the effective volumetric discharge A_Q (eq. 8), modulated by precipitation P(x,z) with each terrain characterized by a distinct h_0 .

Our inversion assuming that water discharge simply scales with only drainage area (A) accurately recovers landscape parameters for $h_0 < 0.5\,\mathrm{km}$. For h_0 values above 0.5 km, retrieval inaccuracies increase, worsening with larger values (Figs. 3A3 & 2B3). However, when we use A_Q (eq. 8) in our inversion, it accurately retrieves the correct landscape parameters, effectively determining elevation, uplift (Fig. 3A3), and m, n and a_s (Fig. S4). The ability of our inversion to

accurately retrieve landscape parameters is particularly noteworthy given that A_Q undergoes significant changes as the landscape evolves with time and we use the values from the final timestep.

4.3.2.4 Lithology

Lithology is an additional spatially variable parameter influencing landscape evolution. We explore its significance by modeling 50 landscapes each featuring a 20 km wide zone with low erodibility, K_l , varying by up to an order of magnitude from the background erodibility, K_b , $2 \cdot 10^{-5} m^{0.9} yr^{-1}$. The sharp change in erodibility results in landscapes with two distinct topographic highs: one aligned with the imposed uplift pattern and another associated with the low erodibility zone where the ratio of altitudes between these peaks is linked to $\frac{K_l}{K_b}$ (e.g., Figs. 3B4, S5D1 and S5D2).

For $\frac{K_l}{K_b} > 0.5$ our standard inversion performs well, almost unaffected by the addition of a stronger rock section (Fig. 3A4). However, for $\frac{K_l}{K_b} < 0.5$, the standard inversion scheme struggles to accurately capture the current properties of the landscape, and the retrieved uplift values reflect the region of lower erodible domain rather than the imposed uplift field (Fig. 3A4). However, when we invert for erodibility (see section 3.1.3) as well as U^*, m, n and a_s the inversion scheme excels in accounting for elevation and uplift pattern (Figs. 3A4 and S5). In addition, the recovered and imposed erodibility ratio show good agreement (Fig. 3A4) suggesting that our inversion scheme is capable of accounting for spatial changes in rock erodibility.

4.3.2.5 Rock uplift rate

To investigate the impact of non-steady rock uplift rates, we bring a detachment-limited landscape to a steady state and then instantaneously increase the uplift rate by a factor of three, similar to observed changes in uplift history along normal fault systems (e.g., Goren et al., 2014; Smith et al., 2024). We proceed to simulate the landscape for an additional 1.6 million years until it reaches a new equilibrium (calculated using equation (3); Fig. S6) and invert landscapes snapshots retained at intervals of 0.1 million years.

Our inversion responds to the step change in rock uplift rate with a minor increase in RMS values for the retrieved elevation. Conversely, the inversion shows greater deviations in the

recovered uplift pattern and in the m, n and a_s values than in elevation (Figs. 3A5, 3B5 & S7). This is because the inversion effectively compensates with adjustments in other parameters to return accurate elevation values. This illustrates the challenge of determining whether a natural landscape is in steady state based solely on elevation misfits. After about half the time needed to reach equilibrium, the inversion returns values that align with the imposed parameters (Fig. 3A5). This stabilization in parameter retrieval is clearly illustrated by a_s values (incorporating the updated U_0 value) which reach their new steady-state levels approximately 0.8 million years after the step change. We attribute the inversion's ability to retrieve the imposed values before the entire landscape reaches steady state to the fact that a significant portion of the landscape is already in equilibrium, with only the upstream sections of rivers still in transition. This is evidenced by the large misfit values at the river tips, which, unlike in steady-state conditions, are more evenly distributed across the landscape (Fig. S8). We note that we observe a similar pattern in landscapes subjected to temporal changes in uplift pattern over a given time period (Text S2 & Fig. S9).

5 Application to natural landscapes

5.1 Selection of sites

To test the real-world applicability of our inversion scheme, we apply it to both divergent and convergent tectonic settings. For the divergent setting, we analyze six landscapes shaped by normal faults, where our understanding of the crust's flexural response to faulting provides a reliable test bed for assessing our inverted uplift patterns. For the convergent setting, we focus on a well-studied, approximately 200 km-wide section of the Himalayas and compare our results to previous rock uplift estimates derived from geomorphological markers.

5.1.1 Landscapes shaped by normal faults

We apply our inversion methodology to natural landscapes shaped by half-graben border faults, where fault offsets on the order of several kilometers flex the brittle upper crust,

producing a 1D rock uplift field that exponentially decreases with across-strike distance from the fault (Fig. S10; Weissel & Karner, 1989). Thicker and stronger faulted layers typically result in longer uplift decay lengths extending farther into the footwall. This relatively simple pattern makes such settings appealing benchmark cases and has been leveraged in previous geomorphic-tectonic studies (e.g., Goren et al., 2014; Ellis & Barnes, 2015). In addition, we have already shown that our inversion framework can accurately recover similar exponential decay behavior in synthetic landscapes (Figs. 2A1, S11; Text S3). As a result, recovering similar trends in natural landscapes, consistent with the expected flexural response, would provide additional support for the validity of our approach.

To this end, we study six landscapes with varying faulted layer thicknesses (Table S2; Olive

441

442

443

444

445

446

447

448

449

450

451

452

453

454

455

456

457

458

459

460

461

462

463

464

465

466

467

468

et al., 2022): The Paeroa Range (Paeroa fault ,New Zealand), Sandia Mountains (New Mexico, USA), Wassuk Range (Nevada, USA), Wasatch Range (Utah, USA), Lehmi Range (Lehmi Fault, Idaho, USA), and Kipengere Range (Livingstone Fault, Lake Malawi, Tanzania). We analyze river sections located far from fault tips (Densmore et al., 2007; Ellis & Barnes, 2015), ensuring that rock uplift is predominantly a function of distance from the fault, allowing us to use the faster 1-D inversion (see section 3.1.2). We also demonstrate the applicability of our 2-D inversion scheme by applying it to the Lemhi range where the uplift pattern is well-documented and has been shown to diminish southward (Fig. S10; Densmore et al., 2007). We include erodibility variations for the Sandia mountains and Wasatch Range, as these feature distinct lithological domains (Bryant, 1990; Williams & Cole, 2007), which may result in spatially variable erosional properties (Figs. 4C2,5). We assume uniform erodibility in other studied landscapes as these exhibits relatively uniform lithology. Finally, we account for climatic effects in all landscapes by computing river discharge A_0 using eq. (8), based on the average spatial distribution of Global Precipitation Measurement (GPM) over the past 22 years from June 2001-2023 (Huffman et al., 2015). We note that by relying on modern satellite-derived precipitation to compute $A_0(x)$, our analysis assumes that spatial rainfall patterns have remained effectively constant since the landscape reached a quasi-steady state. However, climate fluctuations, such

as those during the Pliocene-Pleistocene (e.g., Lisiecki & Raymo, 2005) could have produced

discharge patterns different from today's, and the inversion results derived under modernclimate assumptions may fall outside the uncertainty intervals presented here.

5.1.2 The Himalayas

We apply our inversion scheme to a well-studied, approximately 200 km-wide section of the Himalayas, where previous studies have identified relatively high rock uplift rates occurring around 100 km from the main Himalayan thrust, with slower uplift rates observed farther away (Burbank et al., 2003; Dal Zilio et al., 2021; Godard et al., 2014; Herman et al., 2010; Lavé & Avouac, 2001; Meade, 2010). We exclude the Siwalik Hills from our analysis as rivers in this region are not predominantly detachment-limited. We also omit Tibetan endorheic catchments north of the Himalayan water divide, as these require separate, higher base levels, which would limit the spatial extent of our analysis.

Our inversion accounts for four distinct erodibility sections, delineated by the main lithological units in the area (Fig. 6C; Carosi et al., 2018). Similarly to the normal fault cases we incorporate climatic patterns in the Himalayas (e.g., Bookhagen & Burbank, 2010), by computing river discharge A_Q using eq (8), based on GPM satellite products in the past 22 years (Fig. 6D; Huffman et al., 2015).

5.2 Inversion of natural landscapes

We use 30 m-DEM of landscapes obtained by the Shuttle Radar Topography Mission (Farr et al., 2007). We extract nodes (pixels) corresponding to major rivers, defined as those draining areas larger than a set threshold and above a set base level elevation (Table S2). These thresholds are carefully selected to balance computational efficiency for the inversion calculations with an accurate representation of the landscape's fluvial sections. For landscapes shaped by normal faults, our aim is to include river nodes that cover the entire decay length of the fault-induced uplift. However, this is often complicated for river nodes near the fault, typically located on hanging wall-facing cliffs that drain small areas or lie underwater. Consequently, we calculate the rivers' distance from the outlet, drainage area, and elevation (O'Callaghan & Mark, 1984), and

rotate their geographical coordinates to align with an along-fault strike and across-fault strike coordinate system. We estimate their connectivity and flow path using the steepest descent algorithm (O'Callaghan & Mark, 1984).

We compute multiple inversion scenarios for each landscape, varying the number of B-spline nodes, ensuring the distance between B-spline nodes is at least 5km (Text S1). We report the inversion that minimizes the Akaike Information Criterion (AIC) (Akaike, 1974; Bishop, 2006). The AIC includes a penalty term to prevent potential overfitting caused by the addition of superfluous parameters to the model (Text S4). We also assume an elevation uncertainty of 30 meters, a value that has been deliberately increased from the reported SRTM dataset uncertainty. This additive inflation addresses our model's limitations in capturing detailed terrain features, as highlighted in the synthetic inversion cases. Employing such an approach is common practice across various parameterizations in physical modeling, aiming to better represent the inherent uncertainties without exhausting every detail (e.g., Anderson, 2007).

5.3 Results

5.3.1 Landscapes shaped by normal faults

We apply our 1D inversion to five landscapes (Figs. 4C1–5) and recover the dimensionless rock uplift pattern (Figs. 4A1-5) that best minimizes the misfit between real and modeled elevation (evaluated by RMS values) and the scatter of river profiles in χ_{UKQ} space (Figs. 4B1-5). We highlight that to convert these dimensionless uplift patterns to physical units, we must specify a reference erodibility constant K_0 and use the inverted value of a_s . However, since K_0 is often poorly constrained in natural settings, we report rock uplift patterns in dimensionless units (see sections 2.2 and 3.2).

In all five normal fault cases, the rock uplift pattern decreases with distance from the fault along the footwall, consistent with the results from our synthetic landscape experiments (Figs. 2A1 and S11). In fact, when we fit our recovered rock uplift and to an exponentially decaying function (e^{-x/α_b}) the fitted wavelengths , α_b , correlate with the thickness of the brittle faulted layer, T_e , (Fig. 4D) as constrained by the maximum depth of recorded seismicity (Arabasz et al., 2016; Olive et al., 2022; Table S2). This correlation appears consistent with the theoretical relationship, $\alpha_b \propto T_e^{3/4}$, although we note that our inferred scaling coefficient amounts to $2~{\rm m}^{\frac{1}{4}}$

which is significantly smaller than the suggested $40 \text{ m}^{\frac{1}{4}}$ coefficient by elastic flexure theory and typical lithospheric properties (Text S5). This order-of-magnitude inconsistency has also been observed in the Inyo Mountains (Anders et al., 1993; Bechtel et al., 1990; Goren et al., 2014; Lowry & Smith, 1994) and likely reflects the effects of inelastic deformation and isostatic adjustments driven by erosion and sediment redistribution—processes not accounted for in the idealized flexure models (Buck, 1988).

The well-studied Wasatch Range landscape provides an additional test case for our method due to the availability of independent thermochronological data that record denudation rates (e.g., Armstrong et al., 2003; Smith et al., 2024; Stock et al., 2009). We compare the uplift pattern retrieved by our inversion—both including and excluding spatial variations in erodibility—to the inverse of apatite fission-track ages (Armstrong et al., 2003), which serves as a first-order proxy for denudation. While these ages would require more rigorous conversion to yield quantitative denudation rates, both comparisons show first-order agreement, with rock uplift rates decreasing away from the fault over a wavelength similar to that recovered in our inversion (Fig. 4A2). We note that while the uplift pattern recovered without accounting for erodibility appears to align more closely with the thermochronological trend, we do not assign specific significance to this match, as the inverse of age provides only a first-order approximation and should not be overinterpreted. More importantly, our inversion captures the position of the most recent flexural hinge zone, approximately 17–20 km from the fault, consistent with independent structural and geomorphic interpretations (Armstrong et al., 2003).

The erodibility values recovered by our inversion across the five major lithologic units in the region (Bryant, 1990; Armstrong, 2003) generally fall within the same order of magnitude, with one notable exception (Fig. 4C4). The undifferentiated Tertiary section in the northeast—composed primarily of weak, fine-grained, and poorly cemented fluvial and lacustrine sediments—stands out with an erodibility value nearly seven times higher than the others. Our estimates for the remaining units are broadly consistent with previous findings. For example, Smith et al. (2024) reported that the rock section in Big Cottonwood Canyon is approximately 0.75 as erodible as that in Little Cottonwood Canyon, aligning with our result that the Precambrian unit is about 0.85 times as erodible as the Tertiary unit (Fig. 4C4).

The Sandia Mountains offer an additional case to test how our inversion performs when accounting for spatial variations in erodibility. Inversions assuming uniform or variable erodibility yield similar uplift wavelengths, but the uniform-erodibility model produces an unrealistic high in the rock uplift field approximately 7 km from the fault coinciding with the presence of limestone (Fig. 4A2, blue line). Allowing erodibility to vary based on local lithology yields a more realistic rock uplift pattern that decays smoothly with distance from the fault (Fig. 4A2, purple line), reduces scatter in χ_{UKO} values (Fig. 4B2), and reveals that the Sandia granite is 2.2 times more erodible than the overlying Madera Formation limestone (Fig. 4C2). This results from the reduced erosion by overland flow on permeable limestone combined with a semi-arid environment further inhibiting chemical weathering (Ott et al., 2023). Because limestone is effectively less erodible than granite, erosion proceeds more slowly preserving greater topographic relief for a given amount of rock uplift. If the inversion does not account for the erodibility contrast, it compensates by assigning artificially high uplift in the regions associated with low erobdailty (Fig. 4A2). This is nicely captured by the synthetic experiments where a low erodibility region yields a local high relief and unrealistically high inverted rock uplift (Fig. 3B4, section 6.1).

We highlight that our inversion method is designed to recover the coefficients controlling the B-spline knots, which can be used to describe rock uplift not only along the rivers utilized in the inversion but also across all catchments feeding those rivers (see section 3.5.1). While this capability is demonstrated in the 1D inversion cases (Figs. 4C1-5), its true strength lies in capturing complex spatial attributes across two dimensions. For example, our 2-D inversion for the Lemhi landscape captures the spatial variations in rock uplift expected near the tip of a normal fault within the Lemhi Range. It shows diminishing uplift within 10 km to the fault tip (Fig. 5A), aligning with previously documented k_{sn} values in the region (Densmore et al., 2007), and a general decrease in uplift with increasing distance from the fault axis (Fig. 5C). These observations demonstrate our model's ability to retrieve two-dimensional variations in rock uplift. We note, however, that the apparent increase in rock uplift in the northernmost part of the domain may reflect over-interpolation by the inversion due to the sparse river network in that region (Fig. 5C).

Lastly, similar to our synthetic landscapes (Figs. 2, S2-5), inverting for uplift patterns yields RMS values that are 2-3 times better than those assuming a uniform rock uplift pattern. This is visually supported by the tight alignment of χ_{UkQ} values around the recovered a_S particularly in the Wassuk range case where χ_{UKQ} values that do not account for uplift gradients form three distinct branches in contrast to the neatly aligned χ_{UKQ} values for the inversion that accounts for uplift variations (Fig. 4B3). Additionally, the average recovered m/n ratio is closer to θ = 0.45, a value considered typical for natural landscapes (Gailleton et al., 2021; Mudd et al., 2014; Snyder et al., 2000). The Wassuk Range shows relatively large deviation with an m/n ratio of 0.22. However, when we invert the landscape while fixing n=1 and m=0.45 we recover an uplift pattern resembling the original with an RMS value larger by 1.4 (Fig. S12).

5.3.2 The Himalayas

We apply our 2D inversion scheme to a 200km wide region of the Himalaya (Fig. 6A), account for modern day precipitation rates (Fig. 6E) and four erodibility values which reflect the major lithological units in the region(Fig. 6D). Our recovered rock uplift pattern reveals a distinct region of uplift approximately 100 km N-NE of the main frontal thrust, extending from the eastern to the western end of the study area (Fig. 6A). This result is consistent with previous estimates showing similar uplift position and wavelength(Fig. 6G), based on fluvial terraces, channel geometry (Lavé & Avouac, 2001), ^{10}Be concentrations in detrital sediments (Godard et al., 2014), Apatite Fission track derived denudation rates (Burbank et al., 2003) and thermokinematic models (Herman et al., 2010). We also identify a second uplift peak near the frontal thrust on the southwestern end, though sparse river coverage and higher uncertainty (Fig. 6C) limit confidence in this interpretation.

In contrast to the Sandia Mountains (Fig. 4A2), where erodibility values exhibited significant contrast and strongly influenced the inverted uplift patterns, the recovered erodibility values in the Himalayas (e.g., Fig. 6D) are relatively uniform, with values within one standard

deviation of each other (Table S3). This suggests that spatial variations in erodibility does not play a major role in shaping the landscape in this section of the Himalayas.

To assess the influence of climate patterns, we performed an additional inversion that excluded the effects of variable precipitation. This inversion resulted in RMS values that were higher by a factor of 1.3 (Fig. 6B), but revealed similar overall features, including a rock uplift peak extending from east to west (Fig. 6F). High precipitations on steep terrain are broadly colocated with the zone of faster rock uplift (Fig. 6E, F & G), indicating that here, climate patterns may not significantly modify the localization of erosion (e.g., Godard et al., 2014).

6 Discussion

6.1 Applicability and limits of the methods: Insights from synthetic landscapes

Our analysis of synthetic landscapes illustrates that hillslope diffusion and sediment transport can reduce the accuracy of recovered rock uplift signals. While sediment transport lengths from natural landscapes could, in principle, help identify where our inversion is likely to succeed or fail, their large variability across grain sizes and even between nearby catchments makes them difficult to constrain (e.g., Pizzuto et al., 2014). Thus, to reduce the effects of sediment transport, we therefore prioritize catchments dominated by bedrock channels, where the model assumptions are more likely to hold (e.g., Perron & Royden, 2013; Wobus et al., 2006). Hillslope diffusion can also influence inversion accuracy, but our synthetic experiments suggest that only very strong diffusion produces noticeable discrepancies between recovered and imposed uplift (Fig. S3), yielding overly smooth topography that is typically recognizable and can be excluded from the type of analysis we propose. We note, however, that our model assumes uniform diffusion rates, which may limit its ability to capture real-world variability and assess how such variability affects the recovery of uplift trends (e.g., Auzet & Ambroise, 1996; Bontemps et al., 2020; Matsuoka, 1998).

In scenarios involving temporal changes in rock uplift, our synthetic landscape experiments show that once more than half the time required to reach equilibrium has elapsed, enough river nodes have adjusted to the new conditions as the uplift signal propagates upstream

(Fig. S8), allowing the inversion to reliably approximate the underlying uplift field(Fig. 3A5). In our simulations, temporal changes are modeled as instantaneous steps while in natural settings, these variations may unfold over extended periods. For example, Smith et al. (2024) used river profiles along the normal fault-bound Wasatch Range, demonstrating that rock uplift rates fluctuate temporally up to threefold within as little as 400 ky suggesting that the landscape may never achieve quasi steady state. When we model changes in uplift rates over comparable durations, our inversion method successfully recovers uplift patterns closely resembling the imposed ones (Text S6; Fig. S13), despite the landscapes being far from steady state. This echoes our findings from instantaneous step changes experiment (Fig. 3A5), confirming that even when landscapes are not in steady state, the inversion can retrieve rock uplift patterns that mirror the imposed ones. This likely indicate that our extracted value of a_s reflects a time-averaged value and an uplift pattern that track the tectonic signal, owing to the nature of the χ_{uKQ} framework, which allows for a more integrative treatment of the river network compared to local metrics such as k_{sn} .

Our synthetic experiments testing the effect of temporal changes in the spatial pattern of rock uplift (as opposed to changes in uplift rate described above) show that when these changes are gradual and slower than ~6 Myr (or generating topography at $< 0.17 \ mm \cdot yr^{-1}$), the method typically captures the imposed uplift patterns (Text S7; Fig. S14). We note, however, that the application of our threshold to natural landscapes is not straightforward, as it depends nonlinearly on factors such as erodibility, concavity, and the specific nature of the uplift change (e.g., Royden & Perron, 2013). That said, temporal changes in the spatial pattern of uplift, for instance those associated with shifting fault dip, probably evolve slower than changes in uplift rate. For example, modifications in fault dip or orientation typically unfold over million-year timescales (Armstrong et al., 2003; Olive & Behn, 2014; Oryan & Buck, 2020), an order of magnitude slower than the timescales over which changes in uplift rate can occur (e.g., Smith et al., 2024).

In scenarios where the imposed and recovered uplift patterns diverge (Fig. 3B), discrepancies arise because our forward model interprets all topographic signals on the basis of steady-state

detachment-limited incision, attributing them to variations in rock uplift. With sediment transport, for example, the additional relief produced by deposited material is interpreted by the inversion as faster uplift rates (Fig. 3B1). Under strong diffusion, the effect is less apparent: elevation increases in some regions and decreases in others, so the overall pattern remains close to the imposed one but with a broader spread of uncertainty (Fig. 3B2). When uplift rates change through time, the inversion recovers artificially fast uplift at the domain edges, where the landscape has already reached steady state and accumulated excess relief, while assigning slower uplift in the interior where knickpoints have not yet propagated (Fig. 3B5). Similarly, when spatial variations in topography or precipitation are imposed, regions of additional relief are again misinterpreted as areas of faster uplift (Fig. 3B4–5). Despite these challenges, we demonstrate that the inversion can account for variations in precipitation and erodibility. This is important because it disentangles climate and erodibility from tectonics, unlike widely used metrics such as k_{sn} (e.g., Castillo et al., 2014; Densmore et al., 2007; Ponza et al., 2010; Su et al., 2017), which cannot directly separate the effects of erodibility from uplift.

6.2 Performance on natural landscapes

Our one-dimensional inversion across five normal-fault landscapes demonstrates that the decay wavelength of rock uplift largely correlates with brittle upper-crust thickness (Fig. 4D), in line with classical elastic-flexure theory (e.g., Goren et al., 2014; Nadai, 1963; Weissel & Karner, 1989) and with thermochronological constraints in the Wasatch Mountains. Extending to two dimensions, our Lemhi Range inversion largely reproduces uplift patterns inferred from steepness-index k_{sn} analyses. In the Himalayas, our 2D inversion reveals a broad uplift peak ~100 km north of the main frontal thrust—consistent with previous estimates from terraces, channel geometry, thermochronology, and ^{10}Be data.

6.2.1 Limitations of the inversion

In spite of the inversion success our method carries a number of limitations. As we stressed before one underlying assumption embedded in our inversion mechanism is that the landscape is in steady state. In reality, some features of the recovered uplift profiles may reflect past temporal fluctuations in rock uplift rather than purely spatial variations (see Text S7; Fig. S14). Disentangling these signals presents a compelling challenge. Fortunately, the Himalayas offer a wealth of geomorphic markers that constrain uplift and denudation over a wide range of timescales including rock uplift estimates from river-profile analyses (Lavé & Avouac, 2001), ^{10}Be concentrations in fluvial sediments (Godard et al., 2014), fission track apatite derived denudation rates (Burbank et al., 2003), and thermokinematic modeling (Herman et al., 2010). Together, these data span from thousands to millions of years and consistently indicate a peak in uplift approximately 100 km north of the Main Frontal Thrust (Fig. 6G). The convergence of these spatial patterns across timescales reinforces the persistence of the tectonic signal and suggests that, at least within our study region, the Himalayan landscape may be approaching a quasi-steady state.

In the case of landscapes shaped by normal faulting, only the Wasatch Range offers constraints on uplift history. Smith et al.(2024) used river network inversions to capture the temporal (ignoring spatial) evolution of rock uplift in the area. They documented substantial fluctuations in Pleistocene rock uplift rates, with up to fivefold changes over intervals as short as 400 kyr. Despite this temporal signal in the landscape, our inversion recovers rock uplift patterns that align with available denudation estimates (Fig. 4A4). This result is consistent with our synthetic landscape experiments, where temporal fluctuations in rock uplift produced only modest distortions in the recovered rock uplift field (Fig. 3B5). Even though we lack similarly detailed temporal constraints for the five other normal fault landscapes analyzed, studies of the Inyo fault suggest more modest variations in uplift history (Goren et al., 2014). If we treat the Wasatch landscape as an upper bound on the rate of uplift fluctuations, this suggests that our remaining results may not be strongly biased by temporal variability and can recover first-order spatial patterns of rock uplift.

While we generally recover rock uplift patterns that align with denudation rates and the first-order flexural wavelength, several of our normal fault inversions display secondary

undulations that pure elastic flexure cannot explain (Nadai, 1963; Weissel & Karner, 1989). In the Pāeroa and Wassuk Ranges, we observe a subtle uplift bump at the distal end of the fault, and in Malawi, fluctuations in inferred rock uplift extend as far as 30 km from the fault. These secondary signals occur far from the fault, in areas where the landscape is characterized by lower topographic relief. This pattern suggests a transition from detachment-limited incision to a regime dominated by sediment deposition and hillslope diffusion. For example, in Pāeroa, lowering the base level by just 20 meters produced a more pronounced uplift bump at the profile's end, with RMS misfits increasing by a factor of 1.8. This behavior echoes our results from synthetic landscapes, where active sediment deposition raises river elevation and yields apparent uplift that exceeds the imposed rock uplift (Fig. 3B1). Unfortunately, in the Wassuk and Malawi landscapes, we are unable to further raise the base level, as doing so would exclude channels closest to the fault, where rock uplift gradients and signal-to-noise are likely highest.

In Malawi, we face an additional limitation: the broad width of the landscape means that the original signal associated with fault formation may not have propagated to its outermost catchments. Using our inverted m, n and a_s parameters, along with estimates of average rock uplift from fault displacement (Accardo et al., 2018) and apatite thermochronology (Mortimer et al., 2016), we estimate that it would take approximately 25 million years for the tectonic signal to propagate across the full width of the landscape (Eq. 3). Since the fault likely formed in the early Miocene (Mortimer et al., 2016), this suggests that the far reaches of the Malawi landscape may not yet fully reflect the tectonic forcing, limiting the accuracy of uplift estimates in these regions.

Another limitation of our inversion arises from the use of B-spline functions to represent spatial variations in uplift (Section 3.1.2). The number of B-spline knots influences the smoothness and resolution of the recovered rock uplift pattern. We use the Akaike Information Criterion (AIC) to select the number of B-spline knots, helping to prevent overfitting by limiting the number of free parameters in the inversion. However, AIC-based selection depends on assumptions about uncertainty in the forward model, a factor that is challenging to constrain in natural landscapes. Furthermore, adequately sampling the full hyperparameter space of knot configurations requires running a large number of inversions, which can be computationally

expensive, especially in 2D settings. For example, in the Himalayan case, we explored this hyperparameter space by running 121 separate inversion scenarios, each with a different number of knots, totaling approximately 2,000 CPU hours.

6.2.2 The effect of erodibility and climate on landscape evolution

Our inversion method appears to recover consistent rock uplift patterns in landscapes even when spatial heterogeneity in erodibility exists. In the Himalayas our inversion suggests that erodibility does not play a major role in shaping the landscape, in agreement with Godard et al.'s (2014) results, who showed that ^{10}Be denudation rates do not correlate with lithology. In the Sandia Mountains, allowing erodibility to vary by lithology removes the artificial high produced by the uniform-erodibility model and yields a smooth, fault-centered uplift profile. The inferred erodibility ratio of approximately 2.2 between more erodible Sandia granite and more resistant Madera Formation limestone explains why carbonate-rich regions erode more slowly and would otherwise appear to uplift less when lithologic variation is not accounted for (Fig. 4A2). In the Wasatch Range, our inferred erodibility (Fig. 4C4) aligns with values constrained in the Little and Big Cottonwood catchments (Smith et al., 2024). It also shows that the Tertiary undifferentiated unit, composed largely of poorly cemented sediments, is more erodible and causes our inverted rock uplift profile to plot higher in comparison to the uniform erodibility case.

Another compelling advantage of our inversion scheme is that it can fold spatial rainfall patterns directly into the forward model and assess, case by case, whether doing so alters the inferred uplift field. Similarly to the normal fault landscapes the effect of climate is limited in the Himalayas, where models that ignore climate still recover the same east-to-west uplift bulge (Fig. 6), consistent with thermochronological and cosmogenic data showing only a weak correlation between denudation and current rainfall patterns in that region (Burbank et al., 2003; Godard et al., 2014). This stands in contrast with the central Andes, where rainfall seems to play a more dominant role in shaping the landscape (Leonard et al., 2023).

Ultimately, the degree to which erodibility, precipitation, and rock uplift influence landscape form depends on their spatial contrasts and overlap. In the Sandia Mountains, the

strong lithologic contrast and its alignment with the local rock uplift field make it essential to include erodibility in the inversion to recover even the first-order pattern (Fig. 4A2). In contrast, in the Himalayas, where high rock uplift are broadly co-located with rainfall, tectonic forcing appears to be the dominant control on topographic form (Fig. 6).

6.3 Future applications of our method

The success of our method in recovering rock uplift patterns while accounting for climatic, lithologic, and tectonic influences suggests it can be extended to other settings where long-term uplift rates are poorly constrained. In particular, it offers a way to untangle these overlapping signals and address the long-standing question of the relative roles of tectonic forcing, climate, and erodibility in shaping orogenic regions such as the Andes and Himalayas. (e.g., Leonard et al., 2023; Montgomery et al., 2001; Whipple, 2009; Molnar & England, 1990). Another potential use of our method is its ability to recover long-term uplift trends from forearc landscapes. Recent studies have shown that geodetically locked regions of subduction megathrusts (e.g., Lindsey et al., 2018; Oryan et al., 2023; Steckler et al., 2016), systematically correlate with long-term uplift patterns recorded in forearc terrain shaped over thousands of years (Jolivet et al., 2020; Madella & Ehlers, 2021; Malatesta et al., 2021; Meade, 2010; Oryan et al., 2024; Saillard et al., 2017). This suggests that our inversion method could help leverage these time-averaged landscape signals to infer persistent and spatially variable, patterns of plate coupling over geomorphic timescales.

7 conclusion

We present a χ_{UKQ} based Bayesian inversion method that recovers nondimensionalized, spatially variable rock uplift and relative erodibility directly from the elevation profile of river networks, separating tectonic, climatic, and lithologic signals. Through synthetic experiments spanning sediment transport, hillslope diffusion, precipitation gradients, lithologic contrasts, and time-variable uplift, we show that the method consistently reproduces imposed uplift fields, even

when landscapes deviate from the ideal detachment-limited endmember. Applied to natural landscapes, our inversion recovers exponential footwall decay consistent with normal-fault flexure, with wavelengths scaling with brittle-crust thickness, and reveals a broad uplift high ~100 km north of the Main Frontal Thrust in the Himalayas, consistent with independent geomorphic and thermochronologic constraints. Together, these results demonstrate that fluvial topography can yield first-order, spatially resolved uplift fields, providing a transferable framework to interrogate the interplay of tectonics, climate, and lithology in shaping landscapes over 10³–10⁶-year timescales. More broadly, our study shows that landscapes themselves can serve as quantitative records of long-term tectonic forcing, offering a new way to probe and isolate crustal deformation signals using only digital elevation models that are readily available.

Variable	Description	First
		introduced
Z	Elevation.	1
t	Time.	1
U	Rock uplift rate.	1
E	Bedrock erosion (incision) rate.	1
А	Drainage area.	1
K	Erodibility.	1
m, n	Exponents controlling area–slope dependence of erosion rate	1
С	Celerity of upstream-propagating knickpoint.	2
τ	Travel time for a knickpoint from base level.	3
θ	Concavity index (= m/n).	4
k_{sn}	Nondimensional channel steepness index.	4
a_s	scaling coefficient in the χ-integral solution.	5
χ	Upstream-integral coordinate (drainage-area weighted).	5
Ao	Reference drainage area used to nondimensionalize A.	6
A*	nondimensional drainage area.	6
U_0, K_o	Constant (in 6) or reference(in 7) values used to nondimensionalize U and K.	6
U*, K*	Nondimensionalize uplift and erobdailty.	7
χ_{uK}	χ adjusted for spatial variability in uplift (U) and erodibility (K).	7
Р	Spatially varying precipitation rate.	8
A_Q	Precipitation-weighted discharge rate	8
A_{0Q}	Reference drainage area used to nondimensionalize ${\cal A}_Q$.	8
A_Q^*	Nondimensional precipitation-weighted discharge.	8
χ_{uKQ}	χ adjusted for spatial variability in uplift (U) and erodibility (K) and	2.2
	Precipitation-weighted discharge (A_Q) .	
Z_m	Modeled river elevation along network from forward model.	9
Z_{obs}	Observed river elevation.	10
φ	L2-norm misfit (cost) between modeled and observed elevation.	10
p _l	Inverted forward-model parameters (a_s , m , n , U^* and K^*).	11
C_D	observation covariance matrix.	11
C_M	a priori covariance matrix of the forward-model parameters.	11
G	Jacobian matrix of partial derivatives of the forward model evaluated at every	12
	iteration I.	

$\dot{d_f}$	Synthetic fluvial deposition rate.	13
$\dot{e_f}$	Synthetic fluvial incision rate.	13
$\dot{e_h}$	Synthetic hillslope erosion rates.	13
β	Azimuth angle of the long axis of the imposed synthetic uplift field.	14
x_o, y_o	Coordinates of the Gaussian center of the imposed synthetic uplift field.	14
σ_x, σ_y	Widths of the imposed synthetic uplift Gaussian along the x and y directions, respectively.	14
RMS	Root mean square misfit.	15
ε	Added synthetic noise level in elevations.	4.2
P _{sl}	Precipitation at sea level for synthetic landscape experiments.	4.3.2.3
h_o	Reference elevation for synthetic landscape experiments.	4.3.2.3
K_l	Erodibility value assigned to the localized zone of reduced erodibility in the synthetic landscape experiments.	4.3.2.4
K_b	Background erodibility value .	4.3.2.4
α_b	Characteristic wavelength of the exponentially decaying rock uplift pattern away from a normal fault.	5.3.1
T_e	Thickness of the brittle (faulted) layer	5.3.1

Table 1 - Notation and Definitions of Parameters.

821 8 Figures

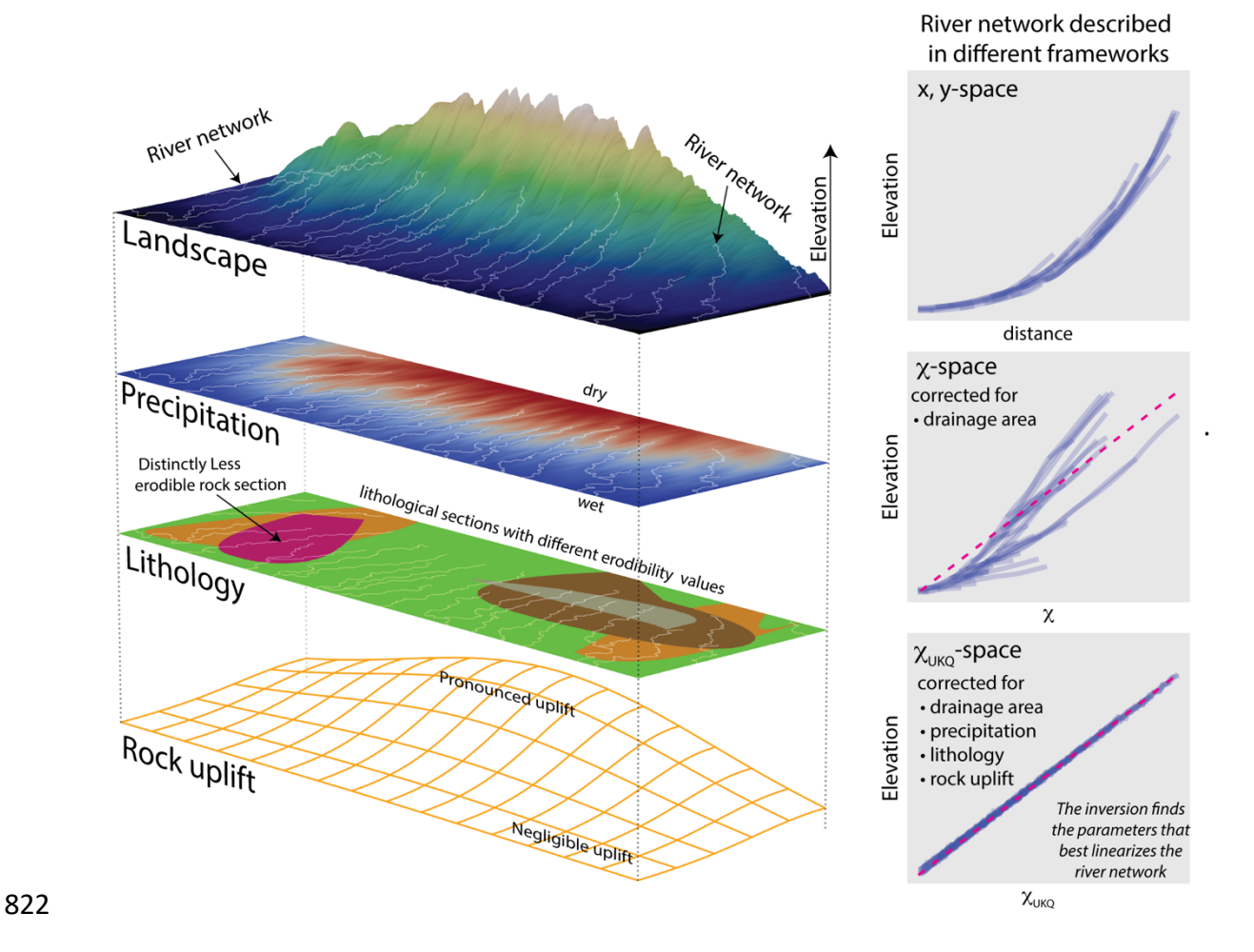


Figure 1 – Illustration of a fluvially-incised landscape and its river networks. Left: Panels depict the tectonic, lithological, and climatic factors shaping the landscape. Right: The river network incising the landscape is described using three geomorphological frameworks, with the lower panel showing the framework used in our approach. The magenta line represents the river network recovered in χ and χ_{UKQ} space.

1D Inversion of detachment limited synthetic landscape ion for 1D spatially varying rock uplift (U(x)) and landscape constants (m,n,as) Inversion for landscape constants (m,n,as) assuming uniform uplift Legend: $\chi_{_{ m UKO}}$ plots for landscape $[U(x), m, n, a_s]$ 0.20 0.2 0.15 Elevation [km] 0.10 0.1 0.05 0.00 200 400 χ_{υκο}[km] 2D Inversion of detachment limited synthetic landscape 20 40 60 80 100 Uavg[] 1 χ_{υκο} plots for landscape RMS=0.01 [U(x,y),m,n,as]0.6 20 Legend: 0.75 [U^{*}(x,y),m,n,as]⁻¹ <u>투</u>0.4 Elevation [km] 40 Elevation 0.50 varying rock uplift (Ư(x,y)) 60 landscape constants (m,n,as) 0.25 0.0 **B2** θ=m/n 0.00 100 $\chi_{\text{UKQ}}[\text{km}]$ 80 100 20 40 60 40 80 60 100 20 20 40 ŝ

Figure 2 – 1D and 2D inversions of detachment limited synthetic landscapes. A – Landscape elevation is shown by colors. Blue curves show river 8000 nodes used in the inversion with curve thickness proportional to the drainage area. Marginal plots show average uplift along each axis. Imposed rock uplift and 500 samples randomly drawn from the inverted rock uplift posterior distribution are shown in red and grey, respectively. B – River nodes plotted in χ_{UKQ} space , derived from the mean inversion solution. Blue and grey denote inversion results accounting for spatial variation in uplift and assuming uniform uplift, respectively. Magenta line shows inverted

D

60

80

Imposed uplift

830 831

832

833

834

835

836

837

60

slope a_s . C and D show imposed and inverted rock uplift solution for the 2D inversion case. Grey lines mark river nodes used to constrain the inversion.

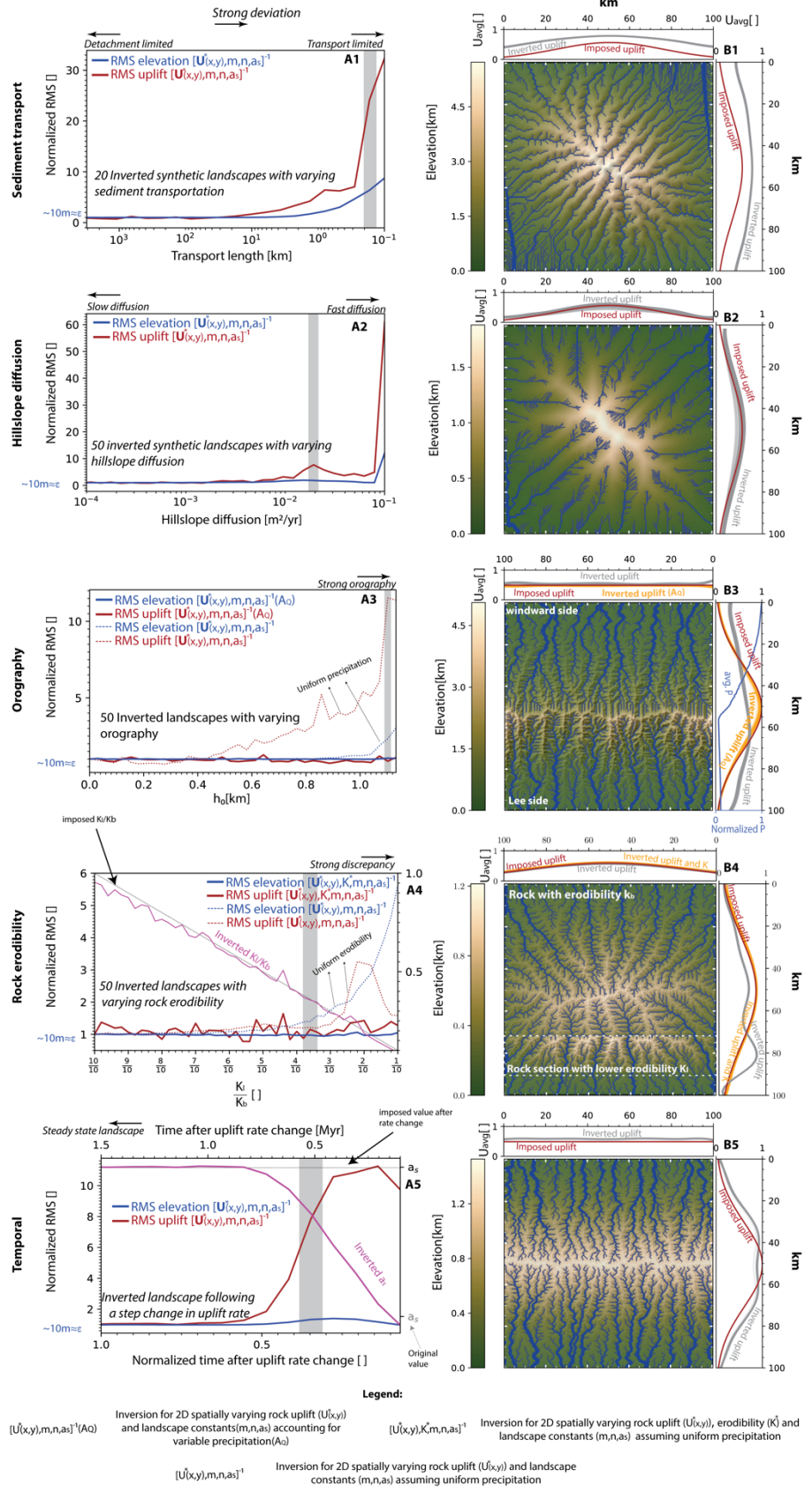


Figure 3 – Inverted synthetic landscapes deviating from the detachment limited model showing varying degrees of sediment deposition (1), hillslope diffusion (2), orographic effects(3), spatial variations in erodibility(4), and temporal changes in uplift rates(5). A - RMS values for elevation and rock uplift and normalized with respect to value obtained for the detachment limited landscape (Fig 1). ε denote the error we introduced amounting to 10m (See section 4.2). Grey vertical line shows an example landscape described in panel B. B -Landscape Elevation. Blue lines show 8000 river nodes used for the inversion with line thickness proportional to the drainage area. Marginal plots show average rock uplift along axis. Imposed rock uplift is shown in red curve and 500 samples randomly drawn from the inverted uplift posterior distribution and extrapolated to the domain are shown in grey and orange colors. The inverted (magenta) and imposed (dashed black line) $\frac{k_l}{k_b}$ and a_s are shown in panel A4 and A5, respectively. The x-axis in Panel A5 displays time in million years (top) and as a fraction of the time it takes for the landscape to reach steady state(bottom).

1D Inverted landscapes shaped by normal faults

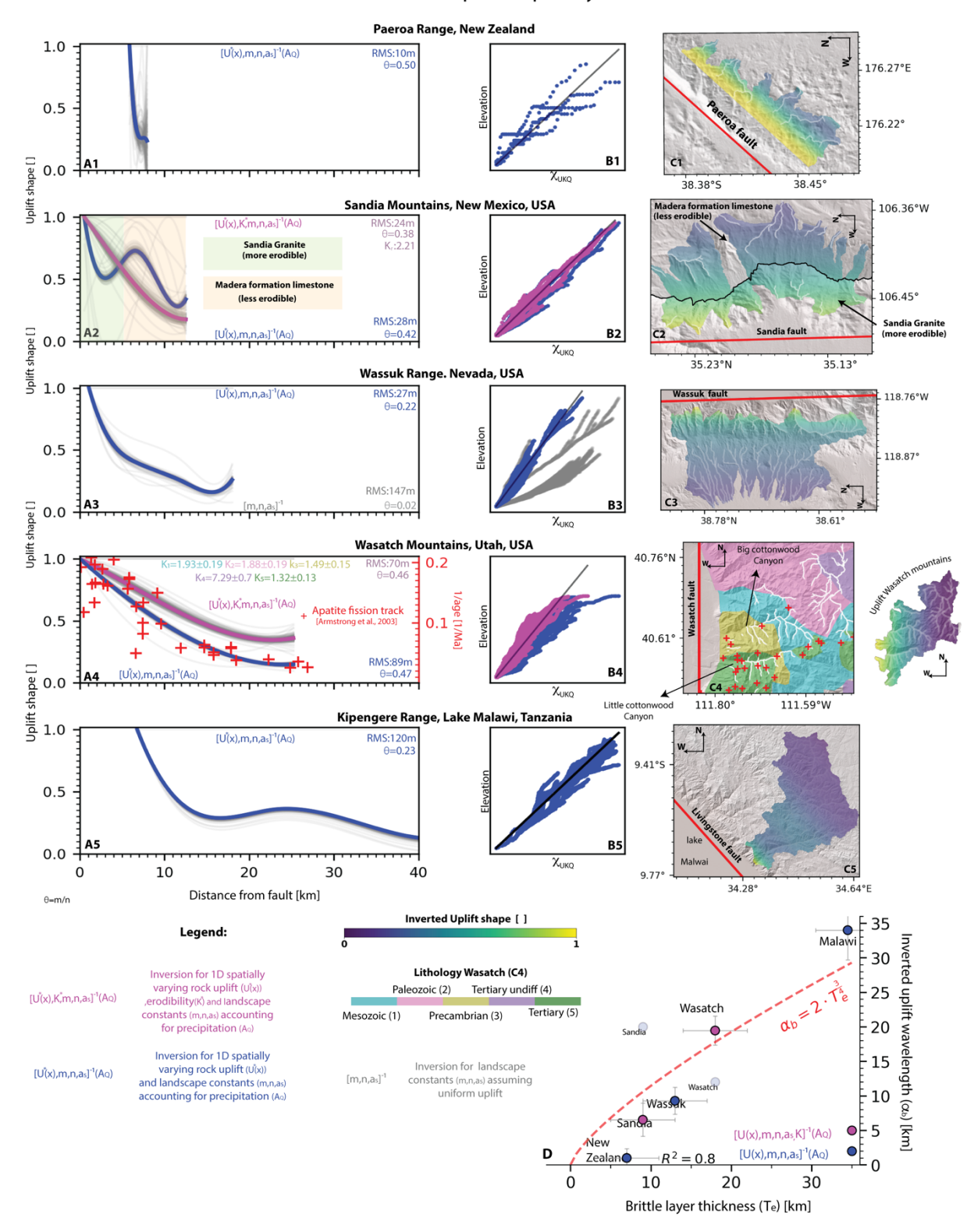


Figure 4 – 1D inversions of five natural landscapes shaped by normal faults. A – Colored and gray curves show the mean and 500 posterior samples rock uplift patterns derived from the inversion solution, respectively. θ denotes inverted m/n. Red markers in A4 are the inverse of apatite fission track ages in the Wasatch Mountains (Armstrong et al., 2003). K_r indicate the inverted erodibility ratio of granite and limestone. B - Colored curves represent river nodes in χ_{UKQ} space obtained using mean inversion solution. Black line shows inverted slope a_s . C – Mean inverted uplift is shown within catchments draining to rivers (highlighted in white) used in the inversion . C2 – Lithologic sections on either side of the black ridgeline (Williams & Cole, 2007). C4 – Simplified lithologic section adapted from Bryant (1990).D - Brittle layer thickness (T_e) and inverted uplift wavelength (α_b) for each of the five 1D landscapes. The red curve shows the best-fitting trend between α_b and $T_e^{3/4}$.

2D inversion of the Lemhi Range (Idaho, USA) landscape shaped by the Lemhi normal fault

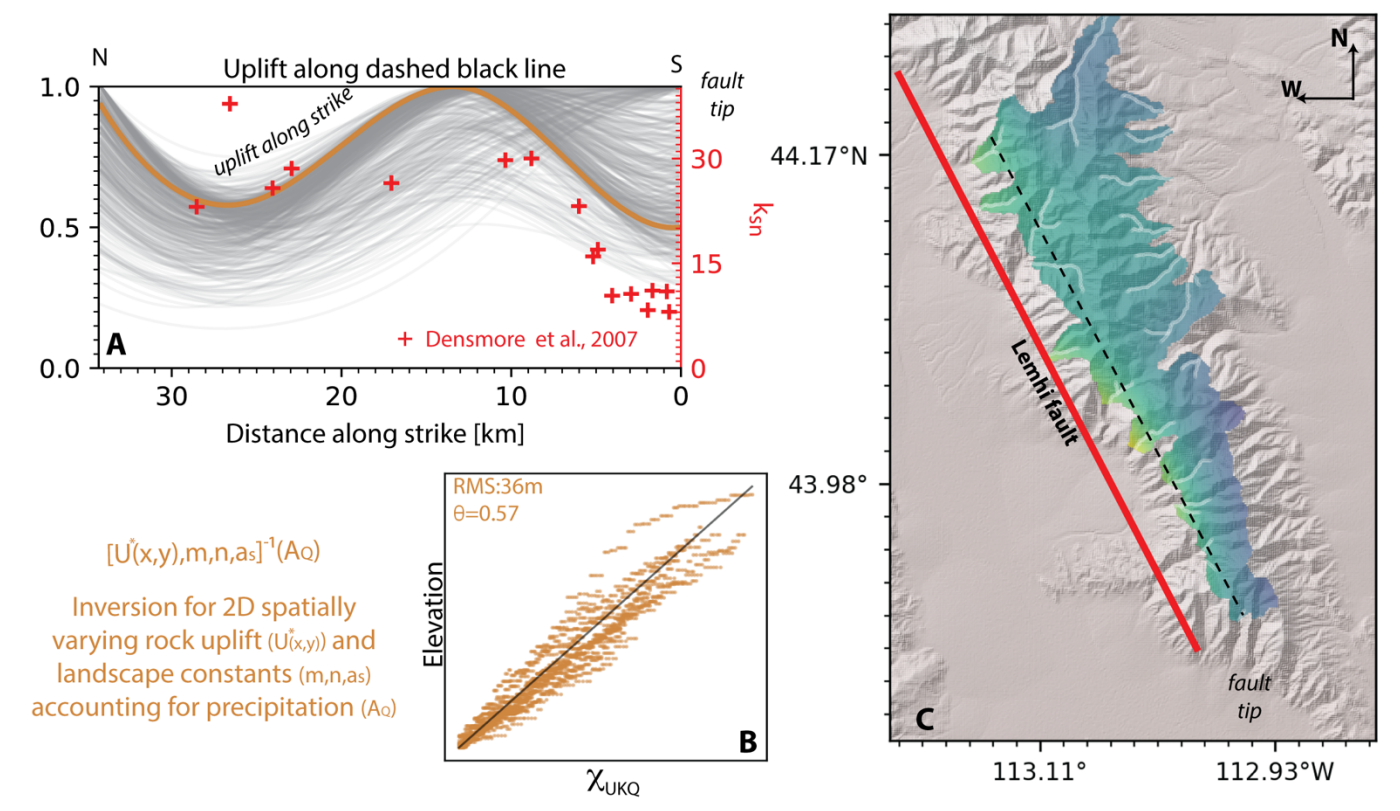


Figure 5 – 2D inversion of Lemhi range shaped by the Lemhi normal fault. A – mean inverted rock uplift (orange curve) and 500 posterior rock uplift soultions (grey curves) shown along the dashed black line in Panel C. Red markers show k_{sn} values (Densmore et al., 2007). B - Colored curves represent river nodes in χ_{UKQ} space obtained using the mean inversion solution. Black line shows inverted slope a_s . θ denotes inverted m/n. C – Mean inverted rock uplift is shown within catchments draining to rivers (highlighted in white) used in the inversion. Dashed line corresponds to the profile shown in A.

Inverted Himalaya landscape

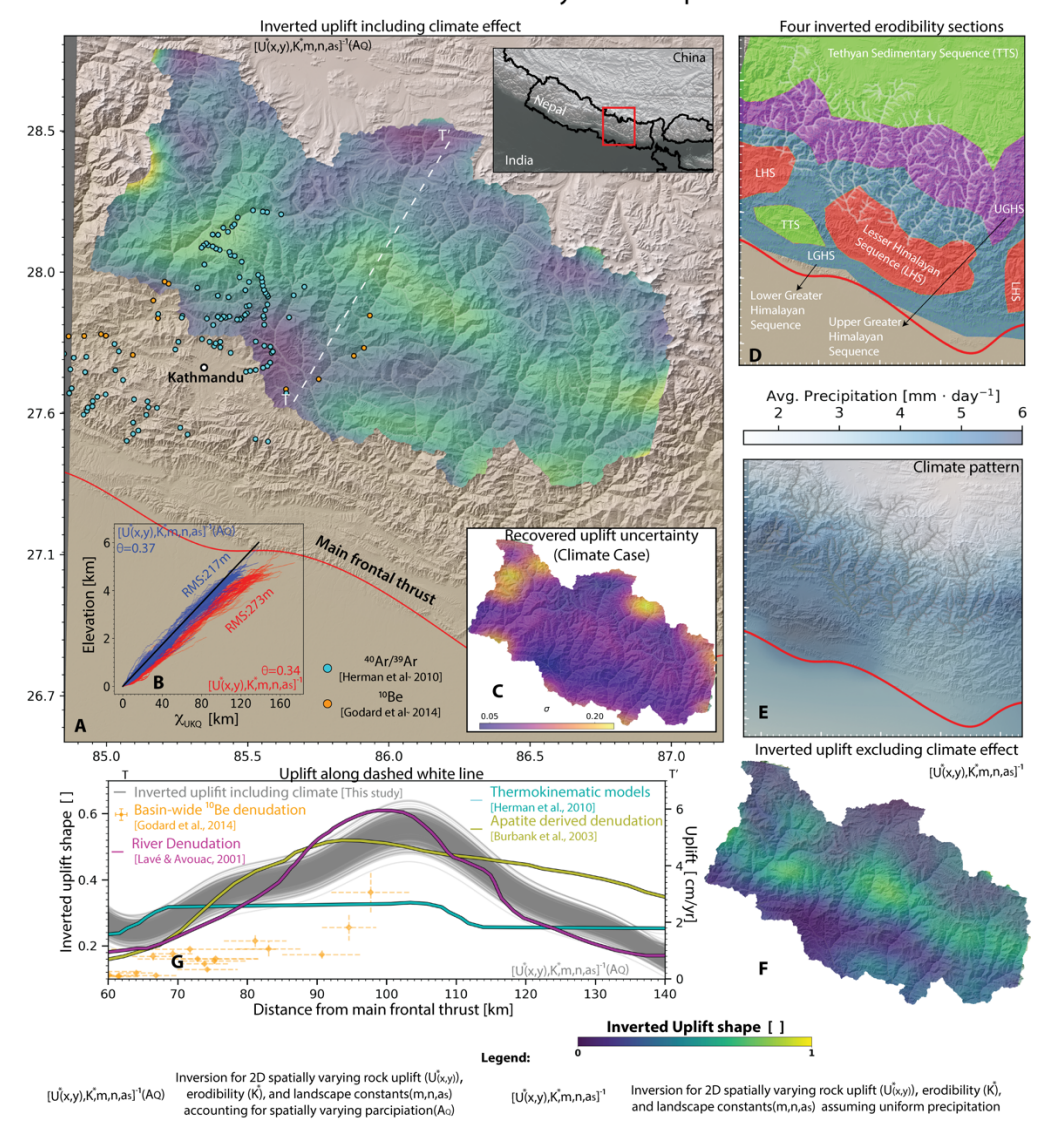


Figure 6 – Inversion results for Himalaya landscape. A – Mean rock uplift pattern within catchments of rivers used in the inversion, with rivers highlighted in white. Positions of $^{40}Ar/^{39}Ar$ and ^{10}Be samples used to constrain incision rates are shown by colored dots. B – Blue and red curves represent rivers in χ_{UKQ} space derived from the mean solution of inversions that include spatially variable precipitation and uniform precipitation, respectively. Black line marks the best fitting inverted slope a_s . θ denotes inverted m/n. C- Rock uplift standard deviation estimated from 500 samples randomly drawn from the posterior distribution. D – Four lithological sections (Carosi et al., 2018) used to constrain the spatial variability of inverted erodibility values. Rivers are marked by white lines. E – Average precipitation used to constrain river discharge A_Q (eq. 8). Rivers are shown by gray lines. F – best fitting rock uplift pattern for the inversion assuming uniform rainfall. G– Gray curves represent 500 rock uplift patterns randomly drawn from the posterior distribution along the dashed white line in panel A. Denudation rates constrained by ^{10}Be (Godard et al., 2014), river profiles (Lavé & Avouac, 2001),

thermokinematic models (Herman et al., 2010) and Apatite Fission Track ages (Burbank et al., 2003) are shown by colored curves.

9 Funding

This work was funded by the Emergence(s)–Ville de Paris Program Project "Inelasticity in the Subduction earthquake cycle" (J.-A.O., B.O.); the French Agence Nationale de la Recherche (ANR) grant GeoSigMA (J.-A.O.), the European Research Council (ERC) under the European Union's Horizon 2020 research and innovation program, Geo-4D project, grant agreement 758210 (R.J.); institut Universitaire de France (R.J.); H2020 European Research council, grant no. 803721 (B.G.); Chateaubriand Fellowship Program, Green Postdoctoral Scholarship from IGPP at SIO and national Science Foundation, grant no. NSF-OAC- 2311208 (B.O.)

909

900

901 902

903

904

905

906

907

908

10 Open Research

911

912

913

914

915

916

917

918

919

920

921

922

910

The Digital Elevation Models (DEMs) utilized in this study were sourced from the Shuttle Radar Topography Mission (Farr al., 2007) freely available and are at https://www.opentopography.org/. Precipitation data were obtained from the NASA Global Precipitation Measurement mission (Huffman et al., 2015), accessible at https://disc.gsfc.nasa.gov/datasets/GPM 3IMERGM 07/summary?keywords=%22IMERG%20fi nal%22. Synthetic landscapes were generated using CHONK (Gailleton et al., 2024). Figures were produced using GMT (Wessel et al., 2019), Matplotlib (Caswell et al., 2021) and Adobe Illustrator (https://www.adobe.com/products/illustrator.html).The DEMs , precipitation data, and code used for the inversion in this paper are freely accessible at https://zenodo.org/records/14029506 (Oryan, 2024). Example scripts and the latest codebase can be found https://github.com/baroryan/ChInversionLandscpes

923

11 Acknowledgments

925

926

927

924

We thank Joel Scheingross, one anonymous reviewer, and our editors for their careful and constructive feedback on our manuscript. Their insights have significantly improved the quality

- and clarity of the paper. We would also like to thank J.-P. Avouac for prolific discussions which contributed to the ideas presented here.
- 930 12 Conflict of Interest Statement
- 931 The authors have no conflicts of interest to disclose.

932 13 References

- Agrapart, Q., & Batailly, A. (2020). Cubic and bicubic spline interpolation in Python. École
- 934 *Polytechnique de Montréal.*, 52. https://doi.org/ffhal-03017566v2
- 935 Akaike, H. (1974). A new look at the statistical model identification. *IEEE Transactions on*
- 936 Automatic Control, 19(6), 716–723. https://doi.org/10.1109/TAC.1974.1100705
- 937 Anders, M. H., Spiegelman, M., Rodgers, D. W., & Hagstrum, J. T. (1993). The growth of fault-
- 938 bounded tilt blocks. *Tectonics*, 12(6), 1451–1459. https://doi.org/10.1029/93TC01547
- Anderson, J. L. (2007). An adaptive covariance inflation error correction algorithm for ensemble
- 940 filters. Tellus A: Dynamic Meteorology and Oceanography, 59(2), 210.
- 941 https://doi.org/10.1111/j.1600-0870.2006.00216.x
- 942 Arabasz, W. J., Pechmann, J. C., & Burlacu, R. (2016). A uniform moment magnitude earthquake
- catalog and background seismicity rates for the Wasatch Front and surrounding Utah
- region. Appendix E of Earthquake Probabilities for the Wasatch Front Region in Utah,
- 945 *Idaho, and Wyoming: Utah Geological Survey Miscellaneous Publication, 16*(3).
- 946 Armijo, R., Meyer, B., King, G. C. P., Rigo, A., & Papanastassiou, D. (1996). Quaternary
- evolution of the Corinth Rift and its implications for the Late Cenozoic evolution of the
- 948 Aegean. Geophysical Journal International, 126(1), 11–53.
- 949 https://doi.org/10.1111/j.1365-246X.1996.tb05264.x
- 950 Armstrong, P. A., Ehlers, T. A., Chapman, D. S., Farley, K. A., & Kamp, P. J. J. (2003).
- Exhumation of the central Wasatch Mountains, Utah: 1. Patterns and timing of exhumation
- deduced from low-temperature thermochronology data. *Journal of Geophysical Research*:
- 953 *Solid Earth*, 108(B3). https://doi.org/10.1029/2001JB001708

- Babault, J., Viaplana-Muzas, M., Legrand, X., Van Den Driessche, J., González-Quijano, M., &
- 955 Mudd, S. M. (2018). Source-to-sink constraints on tectonic and sedimentary evolution of
- 956 the western Central Range and Cenderawasih Bay (Indonesia). Journal of Asian Earth
- 957 *Sciences*, 156, 265–287. https://doi.org/10.1016/j.jseaes.2018.02.004
- 958 Bechtel, T. D., Forsyth, D. W., Sharpton, V. L., & Grieve, R. A. F. (1990). Variations in effective
- elastic thickness of the North American lithosphere. *Nature*, 343(6259), 636–638.
- 960 https://doi.org/10.1038/343636a0
- 961 Bishop, C. M. (2006). Pattern recognition and machine learning (Vol. 4). Springer. Retrieved
- 962 from https://link.springer.com/book/9780387310732
- Bookhagen, B., & Burbank, D. W. (2010). Toward a complete Himalayan hydrological budget:
- Spatiotemporal distribution of snowmelt and rainfall and their impact on river discharge.
- 965 Journal of Geophysical Research: Earth Surface, 115(F3).
- 966 https://doi.org/10.1029/2009JF001426
- 967 Bryant, B. (1990). Geologic map of the Salt Lake City 30'X 60" quadrangle, north-central Utah,
- and Uinta County, Wyoming.
- 969 Buck, W. R. (1988). flexural rotation of normal faults. Tectonics, 7(5), 959–973.
- 970 https://doi.org/10.1029/TC007i005p00959
- 971 Burbank, D. W., Blythe, A. E., Putkonen, J., Pratt-Sitaula, B., Gabet, E., Oskin, M., et al. (2003).
- Decoupling of erosion and precipitation in the Himalayas. *Nature*, 426(6967), 652–655.
- 973 https://doi.org/10.1038/nature02187
- Orange Campforts, B., Vanacker, V., Herman, F., Vanmaercke, M., Schwanghart, W., Tenorio, G. E., et
- al. (2020). Parameterization of river incision models requires accounting for environmental

- heterogeneity: insights from the tropical Andes. *Earth Surface Dynamics*, 8(2), 447–470.
- 977 https://doi.org/10.5194/esurf-8-447-2020
- 978 Carosi, R., Montomoli, C., & Iaccarino, S. (2018). 20 years of geological mapping of the
- 979 metamorphic core across Central and Eastern Himalayas. Earth-Science Reviews, 177,
- 980 124–138. https://doi.org/10.1016/j.earscirev.2017.11.006
- 981 Carretier, S., Martinod, P., Reich, M., & Godderis, Y. (2016). Modelling sediment clasts transport
- 982 during landscape evolution. Earth Surface Dynamics, 4(1), 237–251.
- 983 https://doi.org/10.5194/esurf-4-237-2016
- 984 Castillo, M., Muñoz-Salinas, E., & Ferrari, L. (2014). Response of a landscape to tectonics using
- channel steepness indices (ksn) and OSL: A case of study from the Jalisco Block, Western
- 986 Mexico. *Geomorphology*, 221, 204–214. https://doi.org/10.1016/j.geomorph.2014.06.017
- 987 Caswell, T. A., Droettboom, M., Lee, A., Andrade, E. S. de, Hoffmann, T., Hunter, J., et al. (2021,
- 988 August 13). matplotlib/matplotlib: REL: v3.4.3. [Software] Zenodo.
- 989 https://doi.org/10.5281/zenodo.5194481
- 990 Cattin, R., & Avouac, J. P. (2000). Modeling mountain building and the seismic cycle in the
- 991 Himalaya of Nepal. Journal of Geophysical Research: Solid Earth, 105(B6), 13389-
- 992 13407. https://doi.org/10.1029/2000JB900032
- 993 Cooke, M. L., Crider, J. G., Morell, K. D., Karlstrom, L., & Yanites, B. J. (2025). What Is the
- Energy Budget of Subduction Zone Hazards? Reviews of Geophysics, 63(2),
- 995 e2024RG000848. https://doi.org/10.1029/2024RG000848
- 996 Cordonnier, G., Bovy, B., & Braun, J. (2019). A versatile, linear complexity algorithm for flow
- routing in topographies with depressions. Earth Surface Dynamics, 7(2), 549–562.
- 998 https://doi.org/10.5194/esurf-7-549-2019

- 999 Croissant, T., & Braun, J. (2014). Constraining the stream power law: a novel approach combining
- a landscape evolution model and an inversion method. Earth Surface Dynamics, 2(1), 155–
- 1001 166. https://doi.org/10.5194/esurf-2-155-2014
- Dal Zilio, L., Hetényi, G., Hubbard, J., & Bollinger, L. (2021). Building the Himalaya from
- tectonic to earthquake scales. Nature Reviews Earth & Environment, 2(4), 251–268.
- 1004 https://doi.org/10.1038/s43017-021-00143-1
- Davy, P., & Lague, D. (2009). Fluvial erosion/transport equation of landscape evolution models
- revisited. Journal of Geophysical Research: Earth Surface, 114(F3).
- 1007 https://doi.org/10.1029/2008JF001146
- De Boor, C. (1978). A practical guide to splines (Vol. 27). springer-verlag New York.
- Densmore, A. L., Gupta, S., Allen, P. A., & Dawers, N. H. (2007). Transient landscapes at fault
- 1010 tips. Journal of Geophysical Research, 112(F3), F03S08.
- 1011 https://doi.org/10.1029/2006JF000560
- Dublanchet, P., & Olive, J.-A. (2024). Inelastic deformation accrued over multiple seismic cycles:
- Insights from an elastic-plastic slider-and-springboard model. Seismica, 3(2).
- 1014 https://doi.org/10.26443/seismica.v3i2.1345
- Ellis, M. A., & Barnes, J. B. (2015). A global perspective on the topographic response to fault
- growth. Geosphere, 11(4), 1008–1023. https://doi.org/10.1130/GES01156.1
- 1017 Faccenna, C., Glišović, P., Forte, A., Becker, T. W., Garzanti, E., Sembroni, A., & Gvirtzman, Z.
- 1018 (2019). Role of dynamic topography in sustaining the Nile River over 30 million years.
- 1019 Nature Geoscience, 12(12), 1012–1017. https://doi.org/10.1038/s41561-019-0472-x

- Farr, T. G., Rosen, P. A., Caro, E., Crippen, R., Duren, R., Hensley, S., et al. (2007). The Shuttle
- 1021 Radar Topography Mission. Reviews of Geophysics, 45(2) [Dataset].
- https://doi.org/10.1029/2005RG000183
- Fox, M., Goren, L., May, D. A., & Willett, S. D. (2014). Inversion of fluvial channels for paleorock
- uplift rates in Taiwan. Journal of Geophysical Research: Earth Surface, 119(9), 1853-
- 1025 1875. https://doi.org/10.1002/2014JF003196
- Gailleton, B., Sinclair, H. D., Mudd, S. M., Graf, E. L. S., & Matenco, L. C. (2021). Isolating
- Lithologic Versus Tectonic Signals of River Profiles to Test Orogenic Models for the
- Eastern and Southeastern Carpathians. Journal of Geophysical Research: Earth Surface,
- 1029 *126*(8), e2020JF005970. https://doi.org/10.1029/2020JF005970
- Gailleton, Boris, Mudd, S. M., Clubb, F. J., Grieve, S. W. D., & Hurst, M. D. (2021). Impact of
- 1031 Changing Concavity Indices on Channel Steepness and Divide Migration Metrics. *Journal*
- of Geophysical Research: Earth Surface, 126(10), e2020JF006060.
- 1033 https://doi.org/10.1029/2020JF006060
- Gailleton, Boris, Malatesta, L. C., Cordonnier, G., & Braun, J. (2024). CHONK 1.0: landscape
- evolution framework: cellular automata meets graph theory. Geoscientific Model
- 1036 Development, 17(1), 71–90 [Software]. https://doi.org/10.5194/gmd-17-71-2024
- 1037 Gallen, S. F., Seymour, N. M., Glotzbach, C., Stockli, D. F., & O'Sullivan, P. (2023). Calabrian
- forearc uplift paced by slab-mantle interactions during subduction retreat. *Nature*
- 1039 Geoscience, 16(6), 513–520. https://doi.org/10.1038/s41561-023-01185-4
- Godard, V., Burbank, D. W., Bourlès, D. L., Bookhagen, B., Braucher, R., & Fisher, G. B. (2012).
- 1041 Impact of glacial erosion on ¹⁰ Be concentrations in fluvial sediments of the Marsyandi

- 1042 catchment, central Nepal. Journal of Geophysical Research: Earth Surface, 117(F3),
- 1043 2011JF002230. https://doi.org/10.1029/2011JF002230
- Godard, V., Bourles, D. L., Spinabella, F., Burbank, D. W., Bookhagen, B., Fisher, G. B., et al.
- 1045 (2014). Dominance of tectonics over climate in Himalayan denudation. *Geology*, 42(3),
- 1046 243–246. https://doi.org/10.1130/G35342.1
- Goren, L., Fox, M., & Willett, S. D. (2014). Tectonics from fluvial topography using formal linear
- inversion: Theory and applications to the Inyo Mountains, California. Journal of
- 1049 Geophysical Research: Earth Surface, 119(8), 1651–1681.
- 1050 https://doi.org/10.1002/2014JF003079
- Goren, Liran, Fox, M., & Willett, S. D. (2022). Linear Inversion of Fluvial Long Profiles to Infer
- Tectonic Uplift Histories. In *Treatise on Geomorphology* (pp. 225–248). Elsevier.
- https://doi.org/10.1016/B978-0-12-818234-5.00075-4
- Hack, J. T. (1973). Stream-profile analysis and stream-gradient index. U.S. Geological Survey.
- Harel, M.-A., Mudd, S. M., & Attal, M. (2016). Global analysis of the stream power law
- parameters based on worldwide 10Be denudation rates. Geomorphology, 268, 184–196.
- 1057 https://doi.org/10.1016/j.geomorph.2016.05.035
- Hergarten, S., & Robl, J. (2022). The linear feedback precipitation model (LFPM 1.0) a simple
- and efficient model for orographic precipitation in the context of landform evolution
- 1060 modeling. Geoscientific Model Development, 15(5), 2063–2084.
- 1061 https://doi.org/10.5194/gmd-15-2063-2022
- Herman, F., Copeland, P., Avouac, J.-P., Bollinger, L., Mahéo, G., Le Fort, P., et al. (2010).
- Exhumation, crustal deformation, and thermal structure of the Nepal Himalaya derived
- from the inversion of thermochronological and thermobarometric data and modeling of the

1065 Journal Research: Solid 115(B6). topography. of Geophysical Earth, https://doi.org/10.1029/2008JB006126 1066 1067 Holtmann, R., Cattin, R., Simoes, M., & Steer, P. (2023). Revealing the hidden signature of fault slip history in the morphology of degrading scarps. Scientific Reports, 13(1), 3856. 1068 1069 https://doi.org/10.1038/s41598-023-30772-z 1070 Howard, A. D., & Kerby, G. (1983). Channel changes in badlands. GSA Bulletin, 94(6), 739–752. https://doi.org/10.1130/0016-7606(1983)94%253C739:CCIB%253E2.0.CO;2 1071 1072 Huffman, G. J., Bolvin, D. T., Braithwaite, D., Hsu, K., Joyce, R., Xie, P., & Yoo, S.-H. (2015). 1073 NASA global precipitation measurement (GPM) integrated multi-satellite retrievals for 1074 GPM (IMERG). Algorithm Theoretical Basis Document (ATBD) Version, 4(26), 30. 1075 [Dataset]. Jolivet, R., Simons, M., Duputel, Z., Olive, J., Bhat, H. S., & Bletery, Q. (2020). Interseismic 1076 1077 loading of subduction megathrust drives long term uplift in northern Chile, 1–21. 1078 https://doi.org/10.1029/2019GL085377 1079 King, G. C. P., Stein, R. S., & Rundle, J. B. (1988). The Growth of Geological Structures by Repeated Earthquakes 1. Conceptual Framework. Journal of Geophysical Research: Solid 1080 1081 Earth, 93(B11), 13307–13318. https://doi.org/10.1029/JB093iB11p13307 Kirby, E., & Whipple, K. X. (2012). Expression of active tectonics in erosional landscapes. 1082 1083 Journal of Structural Geology, 44, 54–75. https://doi.org/10.1016/j.jsg.2012.07.009 1084 Lavé, J., & Avouac, J. P. (2001). Fluvial incision and tectonic uplift across the Himalayas of central 1085 Nepal. Journal of Geophysical Research: Solid Earth, 106(B11), 26561–26591.

https://doi.org/10.1029/2001JB000359

1087 Leonard, J. S., & Whipple, K. X. (2021). Influence of Spatial Rainfall Gradients on River 1088 Longitudinal Profiles and the Topographic Expression of Spatially and Temporally 1089 Variable Climates in Mountain Landscapes. Journal of Geophysical Research: Earth Surface, 126(12), e2021JF006183. https://doi.org/10.1029/2021JF006183 1090 Leonard, J. S., Whipple, K. X., & Heimsath, A. M. (2023). Isolating climatic, tectonic, and 1091 1092 lithologic controls on mountain landscape evolution. Science Advances, 9(3), eadd8915. 1093 https://doi.org/10.1126/sciadv.add8915 1094 Lindsey, E. O., Almeida, R., Mallick, R., Hubbard, J., Bradley, K., Tsang, L. L. H., et al. (2018). 1095 Structural Control on Downdip Locking Extent of the Himalayan Megathrust. Journal of Geophysical 1096 Research: Solid Earth, 123(6), 5265-5278. https://doi.org/10.1029/2018JB015868 1097 Lisiecki, L. E., & Raymo, M. E. (2005). A Pliocene-Pleistocene stack of 57 globally distributed 1098 1099 benthic δ18O records. *Paleoceanography*, 20(1). https://doi.org/10.1029/2004PA001071 1100 Lowry, A. R., & Smith, R. B. (1994). Flexural rigidity of the Basin and Range-Colorado Plateau-Rocky Mountain transition from coherence analysis of gravity and topography. *Journal of* 1101 1102 Geophysical Research: Solid Earth, 99(B10), 20123–20140. 1103 https://doi.org/10.1029/94JB00960 Madella, A., & Ehlers, T. A. (2021). Contribution of background seismicity to forearc uplift. 1104 1105 *Nature Geoscience*, 1–6. https://doi.org/10.1038/s41561-021-00779-0 1106 Malatesta, L. C., Bruhat, L., Finnegan, N. J., & Olive, J.-A. L. (2021). Co-location of the Downdip End of Seismic Coupling and the Continental Shelf Break. Journal of Geophysical 1107 1108 Research: Solid Earth, 126(1), e2020JB019589. https://doi.org/10.1029/2020JB019589

1109	Meade, B. J. (2010). The signature of an unbalanced earthquake cycle in Himalayan topography?
1110	Geology, 38(11), 987–990. https://doi.org/10.1130/G31439.1
1111	Melnick, D. (2016). Rise of the central Andean coast by earthquakes straddling the Moho. <i>Nature</i>
1112	Geoscience, 9(5), 401-407. https://doi.org/10.1038/ngeo2683
1113	Merritt, W. S., Letcher, R. A., & Jakeman, A. J. (2003). A review of erosion and sediment transport
1114	models. Environmental Modelling & Software, 18(8), 761–799.
1115	https://doi.org/10.1016/S1364-8152(03)00078-1
1116	Molnar, P., & England, P. (1990). Late Cenozoic uplift of mountain ranges and global climate
1117	change: chicken or egg? Nature, 346(6279), 29-34. https://doi.org/10.1038/346029a0
1118	Mudd, S. M., Attal, M., Milodowski, D. T., Grieve, S. W. D., & Valters, D. A. (2014). A statistical
1119	framework to quantify spatial variation in channel gradients using the integral method of
1120	channel profile analysis. Journal of Geophysical Research: Earth Surface, 119(2), 138-
1121	152. https://doi.org/10.1002/2013JF002981
1122	O'Callaghan, J. F., & Mark, D. M. (1984). The extraction of drainage networks from digital
1123	elevation data. Computer Vision, Graphics, and Image Processing, 28(3), 323-344.
1124	https://doi.org/10.1016/S0734-189X(84)80011-0
1125	Olive, JA., & Behn, M. D. (2014). Rapid rotation of normal faults due to flexural stresses: An
1126	explanation for the global distribution of normal fault dips. Journal of Geophysical
1127	Research: Solid Earth, 119(4), 3722–3739. https://doi.org/10.1002/2013JB010512
1128	Olive, JA., Malatesta, L. C., Behn, M. D., & Buck, W. R. (2022). Sensitivity of rift tectonics to
1129	global variability in the efficiency of river erosion. Proceedings of the National Academy
1130	of Sciences, 119(13), e2115077119. https://doi.org/10.1073/pnas.2115077119

- Oryan, B. (2024). Supplements for Inferring Long-Term Tectonic Uplift Patterns from Bayesian
- 1132 Inversion of Fluvially-Incised Landscapes paper [Data set]. Zenodo.
- https://doi.org/10.5281/zenodo.14029506
- Oryan, B., & Buck, W. R. (2020). Larger tsunamis from megathrust earthquakes where slab dip is
- reduced. *Nature Geoscience*. https://doi.org/10.1038/s41561-020-0553-x
- 1136 Oryan, B., Betka, P. M., Steckler, M. S., Nooner, S. L., Lindsey, E. O., Mondal, D., et al. (2023).
- New GNSS and Geological Data From the Indo-Burman Subduction Zone Indicate Active
- 1138 Convergence on Both a Locked Megathrust and the Kabaw Fault. *Journal of Geophysical*
- 1139 *Research: Solid Earth*, 128(4), e2022JB025550. https://doi.org/10.1029/2022JB025550
- Oryan, B., Olive, J.-A., Jolivet, R., Malatesta, L. C., Gailleton, B., & Bruhat, L. (2024). Megathrust
- locking encoded in subduction landscapes. Science Advances, 10(17), eadl4286.
- 1142 https://doi.org/10.1126/sciadv.adl4286
- Ott, R., Gallen, S. F., & Helman, D. (2023). Erosion and weathering in carbonate regions reveal
- climatic and tectonic drivers of carbonate landscape evolution. Earth Surface Dynamics,
- 1145 *11*(2), 247–257. https://doi.org/10.5194/esurf-11-247-2023
- Perron, J. T., & Royden, L. (2013). An integral approach to bedrock river profile analysis. *Earth*
- 1147 *Surface Processes and Landforms*, 38(6), 570–576. https://doi.org/10.1002/esp.3302
- 1148 Piegl, L., & Tiller, W. (1997). *The NURBS Book*. Springer-Verlag.
- 1149 Pizzuto, J., Schenk, E. R., Hupp, C. R., Gellis, A., Noe, G., Williamson, E., et al. (2014).
- 1150 Characteristic length scales and time-averaged transport velocities of suspended sediment
- in the mid-Atlantic Region, USA. Water Resources Research, 50(2), 790–805.
- https://doi.org/10.1002/2013WR014485

Ponza, A., Pazzaglia, F. J., & Picotti, V. (2010). Thrust-fold activity at the mountain front of the 1153 1154 Northern Apennines (Italy) from quantitative landscape analysis. *Geomorphology*, 123(3), 1155 211–231. https://doi.org/10.1016/j.geomorph.2010.06.008 Pritchard, D., Roberts, G. G., White, N. J., & Richardson, C. N. (2009). Uplift histories from river 1156 profiles. Geophysical Research Letters, 36(24). https://doi.org/10.1029/2009GL040928 1157 1158 Roering, J. J., Kirchner, J. W., & Dietrich, W. E. (1999). Evidence for nonlinear, diffusive sediment transport on hillslopes and implications for landscape morphology. Water 1159 1160 Resources Research, 35(3), 853–870. https://doi.org/10.1029/1998WR900090 Roering, J. J., Kirchner, J. W., Sklar, L. S., & Dietrich, W. E. (2001). Hillslope evolution by 1161 nonlinear creep and landsliding: An experimental study. Geology, 29(2), 143. 1162 https://doi.org/10.1130/0091-7613(2001)029%253C0143:HEBNCA%253E2.0.CO;2 1163 Rosenbloom, N. A., & Anderson, R. S. (1994). Hillslope and channel evolution in a marine 1164 terraced landscape, Santa Cruz, California. Journal of Geophysical Research: Solid Earth, 1165 1166 99(B7), 14013–14029. https://doi.org/10.1029/94JB00048 1167 Saillard, M., Audin, L., Rousset, B., Avouac, J.-P., Chlieh, M., Hall, S. R., et al. (2017). From the 1168 seismic cycle to long-term deformation: linking seismic coupling and Quaternary coastal 1169 geomorphology along the Andean megathrust. Tectonics, *36*(2), 241–256. https://doi.org/10.1002/2016TC004156 1170 1171 Smith, A. G. G., Fox, M., Moore, J. R., Miller, S. R., Goren, L., Morriss, M. C., & Carter, A. 1172 (2024). One Million Years of Climate-Driven Rock Uplift Rate Variation on the Wasatch Fault Revealed by Fluvial Topography. American Journal of Science, 324. 1173 1174 https://doi.org/10.2475/001c.92194

- Snyder, N. P., Whipple, K. X., Tucker, G. E., & Merritts, D. J. (2000). Landscape response to tectonic forcing: Digital elevation model analysis of stream profiles in the Mendocino triple junction region, northern California. *GSA Bulletin*, 112(8), 1250–1263.
- https://doi.org/10.1130/0016-7606(2000)112%253C1250:LRTTFD%253E2.0.CO;2
- Steckler, M. S., Mondal, D. R., Akhter, S. H., Seeber, L., Feng, L., Gale, J., et al. (2016). Locked
- and loading megathrust linked to active subduction beneath the Indo-Burman Ranges.
- 1181 *Nature Geoscience*, 9(8), 615–618. https://doi.org/10.1038/ngeo2760
- Su, Q., Xie, H., Yuan, D.-Y., & Zhang, H.-P. (2017). Along-strike topographic variation of
- Qinghai Nanshan and its significance for landscape evolution in the northeastern Tibetan
- Plateau. Journal of Asian Earth Sciences, 147, 226–239.
- https://doi.org/10.1016/j.jseaes.2017.07.019
- 1186 Tarantola, A. (2005). Inverse Problem Theory and Methods for Model Parameter Estimation.
- Society for Industrial and Applied Mathematics. https://doi.org/10.1137/1.9780898717921
- 1188 Watts, A. B. (2001). Isostasy and Flexure of the Lithosphere. Cambridge University Press.
- 1189 Retrieved from https://books.google.com/books?hl=en&lr=&id=QlUgBqJ6m-
- 1190 MC&oi=fnd&pg=PR11&dq=isostasy&ots=KMIwT-K-82&sig=EEBiI2c-910Do0N-
- 1191 5fBIxEyOtq8
- 1192 Wessel, P., Luis, J. F., Uieda, L., Scharroo, R., Wobbe, F., Smith, W. H. F., & Tian, D. (2019).
- The Generic Mapping Tools Version 6. Geochemistry, Geophysics, Geosystems, 20(11),
- 1194 5556–5564. [Software]. https://doi.org/10.1029/2019GC008515
- 1195 Whipple, K. X. (2009). The influence of climate on the tectonic evolution of mountain belts.
- Nature Geoscience, 2(2), 97–104. https://doi.org/10.1038/ngeo413

1197	Whipple, K. X., & Tucker, G. E. (1999). Dynamics of the stream-power river incision models
1198	Implications for height limits of mountain ranges, landscape response timescales, and
1199	research needs. Journal of Geophysical Research: Solid Earth, 104(B8), 17661-17674.
1200	https://doi.org/10.1029/1999JB900120
1201	Willgoose, G., Bras, R. L., & Rodriguez-Iturbe, I. (1991). A physical explanation of an observed
1202	link area-slope relationship. Water Resources Research, 27(7), 1697–1702.
1203	https://doi.org/10.1029/91WR00937
1204	Williams, P. L., & Cole, J. C. (2007). Geologic Map of the Albuquerque 30' X 60' Quadrangle,
1205	North-central New Mexico (Vol. 2946). US Department of the Interior, US Geological
1206	Survey.
1207	

14 References from the Supporting Information 1209 1210 Agrapart, Q., & Batailly, A. (2020). Cubic and bicubic spline interpolation in Python. École 1211 Polytechnique de Montréal., 52. https://doi.org/ffhal-03017566v2 1212 1213 Arabasz, W. J., Pechmann, J. C., & Burlacu, R. (2016). A uniform moment magnitude earthquake 1214 catalog and background seismicity rates for the Wasatch Front and surrounding Utah region. 1215 Appendix E of Earthquake Probabilities for the Wasatch Front Region in Utah, Idaho, and 1216 Wyoming: Utah Geological Survey Miscellaneous Publication, 16(3). 1217 1218 De Boor, C. (1978). A practical guide to splines (Vol. 27). springer-verlag New York. 1219 1220 Ellis, M. A., & Barnes, J. B. (2015). A global perspective on the topographic response to fault 1221 growth. Geosphere, 11(4), 1008–1023. https://doi.org/10.1130/GES01156.1 1222 1223 Piegl, L., & Tiller, W. (1997). The NURBS Book. Springer-Verlag.